frontiers | Frontiers in Marine Science

TYPE Original Research
PUBLISHED 10 July 2023
DOI 10.3389/fmars.2023.1206062

OPEN ACCESS

EDITED BY
Koji Suzuki,
Hokkaido University, Japan

REVIEWED BY
Lei Lin,
Shandong University of Science and Technology, China
Urmas Lips,
Tallinn University of Technology, Estonia

*CORRESPONDENCE
Jan Kossack
jan.kossack@hereon.de

RECEIVED 14 April 2023
ACCEPTED 19 June 2023
PUBLISHED 10 July 2023

CITATION
Kossack J, Mathis M, Daewel U, Zhang YJ and Schrum C (2023) Barotropic and baroclinic tides increase primary production on the Northwest European Shelf.
Front. Mar. Sci. 10:1206062.
doi: 10.3389/fmars.2023.1206062

Barotropic and baroclinic tides increase primary production on the Northwest European Shelf

Jan Kossack[1]*, Moritz Mathis[1], Ute Daewel[1], Yinglong Joseph Zhang[2] and Corinna Schrum[3]

[1]Institute of Coastal Systems, Helmholtz-Zentrum Hereon, Geesthacht, Germany, [2]Center for Coastal Resource Management, Virginia Institute of Marine Science, College of William & Mary, Gloucester Point, VA, United States, [3]Institute of Oceanography, University of Hamburg, Hamburg, Germany

High biological productivity and the efficient export of carbon-enriched subsurface waters to the open ocean via the continental shelf pump mechanism make mid-latitude continental shelves like the northwest European shelf (NWES) significant sinks for atmospheric CO_2. Tidal forcing, as one of the regionally dominant physical forcing mechanisms, regulates the mixing-stratification status of the water column that acts as a major control for biological productivity on the NWES. Because of the complexity of the shelf system and the spatial heterogeneity of tidal impacts, there still are large knowledge gaps on the role of tides for the magnitude and variability of biological carbon fixation on the NWES. In our study, we utilize the flexible cross-scale modeling capabilities of the novel coupled hydrodynamic–biogeochemical modeling system SCHISM–ECOSMO to quantify the tidal impacts on primary production on the NWES. We assess the impact of both the barotropic tide and the kilometrical-scale internal tide field explicitly resolved in this study by comparing simulated hindcasts with and without tidal forcing. Our results suggest that tidal forcing increases biological productivity on the NWES and that around 16% (14.47 Mt C) of annual mean primary production on the shelf is related to tidal forcing. Vertical mixing of nutrients by the barotropic tide particularly invigorates primary production in tidal frontal regions, whereas resuspension and mixing of particulate organic matter by tides locally hinders primary production in shallow permanently mixed regions. The tidal impact on primary production is generally low in deep central and outer shelf areas except for the southwestern Celtic Sea, where tidal forcing substantially increases annual mean primary production by 25% (1.53 Mt C). Tide-generated vertical mixing of nutrients across the pycnocline, largely attributed to the internal tide field, explains one-fifth of the tidal response of summer NPP in the southwestern Celtic Sea. Our results therefore suggest that the tidal NPP response in the southwestern Celtic Sea is caused by a combination of processes likely including tide-induced lateral on-shelf transport of nutrients. The tidally enhanced turbulent mixing of nutrients fuels new production in the seasonally stratified parts of the NWES, which may impact the air–sea CO_2 exchange on the shelf.

KEYWORDS

NW Europe, tides, internal tides, vertical mixing, primary production, Celtic Sea, Malin-Hebrides shelf, 3D coupled hydrodynamic-biogeochemical modeling

1 Introduction

Continental shelves play an important role in the global carbon cycle. High biological productivity and the efficient export of carbon-enriched waters to the open ocean via the continental shelf pump mechanism (Tsunogai et al., 1999; Thomas et al., 2004) on middle- and high- latitude continental shelves are understood to contribute to globally significant oceanic uptake of atmospheric CO_2 (Frankignoulle and Borges, 2001; Laruelle et al., 2014; Legge et al., 2020). Both the physical and biological components of the continental shelf pump mechanism rely on seasonal stratification and processes specific to the respective shelf environments. Given the complexity of the dynamic shelf systems, there still are considerable knowledge gaps on the role of shelf-specific physical and biogeochemical processes for the magnitude and variability of carbon sequestration on continental shelves.

On the northwest European shelf (NWES; Figure 1A), the biological component of the continental shelf pump mechanism is suggested to be critical for observed carbon sequestration (Legge et al., 2020). Tidal forcing, as one of the regionally dominant physical forcing mechanisms, regulates the mixing-stratification status of the water column that acts as a major control for biological productivity in the shelf system. During seasonal stratification, tidal forcing structures the NWES into shallow permanently mixed regions, transitionary regions with tidal fronts and weak stratification and deep stably stratified regions (Simpson and Hunter, 1974). Each of these tide-induced subsystems feature distinct primary production dynamics (van Leeuwen et al., 2015), in which tidal forcing impacts net primary production (NPP), both positively and negatively, by enhanced vertical mixing of nutrients, biomass, and suspended matter and by causing sediment resuspension (Zhao et al., 2019).

In tidally dominated shelf seas, tides produce turbulence due to friction of tidal currents with the sea bed (Simpson and Hunter, 1974; Rippeth, 2005). This tidally generated turbulence vertically mixes the bottom layer of a stratified shelf system, whereas wind stress and breaking surface waves turbulently mix the surface layer. Bottom-driven tidal mixing is well reproduced by state-of-the-art numerical ocean models (Burchard et al., 2002). Its impact on water column stratification and vertical fluxes is strong in shallow shelf areas where the bottom and surface mixed layers can directly interact. Bottom-driven tidal mixing increases primary production by replenishing nutrients in the surface mixed layer (Hu et al., 2008; Sharples, 2008) but also decreases productivity by degrading light conditions through upward mixing of resuspended sediments (Porter et al., 2010; Capuzzo et al., 2013; Capuzzo et al., 2018) and by promoting dilution that hinders phytoplankton growth (Cloern, 1991). Numerous studies have established local effects of bottom-driven vertical mixing by tides on primary production on the NWES and regionally differing responses to tidal forcing (e.g., Cloern, 1991; Richardson et al., 2000; Sharples, 2008). In their comprehensive modeling study that accounted for tide-modulated benthic–pelagic coupling and lower trophic- level dynamics, Zhao et al. (2019) found a considerable, but spatially heterogeneous, tidal response of primary production in the North Sea. To date, there however is no comparable study that quantifies the tidal response of primary production for the entire NWES while accounting for the spatial heterogeneity of the shelf system.

In addition to bottom-driven vertical mixing, tides can also generate vertical mixing in stratified shelf regions by causing intermittent shear instabilities within the pycnocline (Rippeth, 2005). Tide-related shear instabilities in the pycnocline can be caused by breaking internal tides (Whalen et al., 2020), the interaction of wind-induced inertial oscillations with internal tides (van Haren et al., 1999; Hopkins et al., 2014), or the barotropic tide itself (Becherer et al., 2022). Such pycnocline mixing is crucial for the supply of nutrients for biological productivity in the subsurface biomass maximum (SBM) at the base of the pycnocline (Cullen, 2015). It is suggested that primary production in the SBM is predominantly new production (Hickman et al., 2012), i.e., sustained by allochthonous nutrient sources, and accounts for up to 50% of annual carbon fixation on the NWES

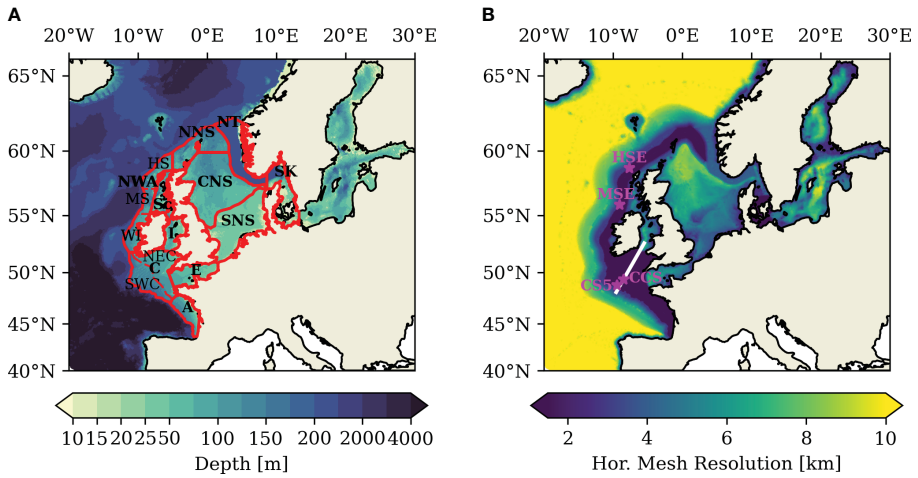

FIGURE 1
(A) Bathymetry in the model domain; red lines delineate subareas. **(B)** Horizontal model resolution of the unstructured triangular grid of the NWES-IT configuration. Magenta stars in **(B)** indicate positions of stations used for validation and analysis. White line in **(B)** indicates transect used in Sect. 3.3.

(Richardson et al., 2000; Rippeth et al., 2009; Hickman et al., 2012). This makes pycnocline mixing a potentially important component of the continental shelf sea pump on the NWES (Rippeth et al., 2014).

Baroclinic tides, also termed internal tides, are generated by a transfer of energy from the barotropic tide to the baroclinic tide through interaction of stratified flow with extreme topography like the shelf break (Baines, 1982). The NWES is a hotspot of internal tide generation, and particularly high tidal energy conversion has been reported for the steep Celtic Sea shelf break (Baines, 1982; Vlasenko et al., 2014). Observational studies have shown intensified pycnocline mixing associated with the internal tide at the shelf break of the NWES (New and Pingree, 1990; Rippeth and Inall, 2002). Low-mode internal tides propagate coherently for hundreds of kilometers across the Celtic Sea (Pingree and New, 1995; Green et al., 2008) and generate shear instabilities in the pycnocline when dissipating. Mixing by internal tides was shown to impact nutrient fluxes and biological productivity in the Celtic Sea (Pingree and Mardell, 1981; Sharples et al., 2007; Sharples et al., 2009; Tweddle et al., 2013). Sparse observations and the high spatial variability and episodic nature of mixing by internal tides however impede a comprehensive analysis and quantification of the role of internal tides for biological carbon fixation on the shelf.

Model- based studies on the other hand face the problem that the reproduction of realistic levels of pycnocline mixing in state-of-the-art numerical ocean models is a difficult task. Commonly implemented turbulence closures only crudely account for the contribution of high-frequency internal waves (Simpson et al., 1996; Burchard et al., 2002; Rippeth, 2005). Recent advances in high-resolution regional ocean modeling have however demonstrated the reproduction of the kilometrical-scale internal tide field on the NWES (Guihou et al., 2018). Graham et al. (2018a) further suggest that increased pycnocline mixing in a kilometrical-scale model configuration improved a bias in the representation of sea surface temperature at the shelf break of the NWES present in a coarser model configuration. Until now, no study has however addressed the implications of the improved representation of the internal tide field for primary production on the shelf.

In this paper, we present a novel coupled physical–biogeochemical regional model framework with kilometrical-scale horizontal resolution for the NWES. The model employs a flexible unstructured horizontal grid that explicitly resolves the low-mode internal tide field generated by the regionally dominant M2 tide in the Celtic Sea and shelf areas along the shelf break. The flexible horizontal grid facilitates coupled physical–biogeochemical simulations at reasonable computational cost and thus enables multiyear model integrations of the entire NWES and adjacent regions in the northeastern Atlantic. We apply the model to for the first time quantify tidal impacts on primary production on the entire NWES and provide a first estimate for the role of internal tides for biological carbon fixation along the shelf break of the NWES. We present the details of the applied model configurations and assess overall model performance in Section 2. In Section 3, we investigate the tidal impacts on primary production and disentangle the contribution of barotropic and baroclinic tides to vertical mixing of nutrients.

2 Materials and methods

2.1 Regional ocean circulation model SCHISM

The open-source community- supported 3D physical modeling system SCHISM (Zhang et al., 2016b) is used in this study. SCHISM is a derivative product built from the original SELFE (Zhang and Baptista, 2008) and distributed with an open-source Apache v2 license. SCHISM is a numerically efficient and robust modeling system designed for the effective cross-scale simulation of 3D baroclinic ocean circulation. SCHISM has been used in multiple studies that span from shallow coastal areas to the deep open ocean (Yu et al., 2017; Ye et al., 2020; Wang Z. et al., 2022), as well as in a study of up/downwelling in shelf break canyons (Wang H. et al., 2022).

SCHISM is based on a customizable triangular–quadrangular unstructured horizontal grid. Flexible local refinement of the unstructured grid allows telescoping high horizontal resolution in areas of specific interest, and vice versa a low resolution in other parts of the domain. This feature facilitates high-resolution coupled ocean-ecosystem simulations at reasonable computational costs. The vertical coordinate is discretized with flexible hybrid Localized Sigma Coordinates with Shaved Cells (LSC^2; Zhang et al., 2015). The LSC^2 vertical coordinate effectively reduces the pressure gradient force error (Zhang et al., 2016b). The LSC^2 vertical coordinate further enables the accurate representation of bathymetry without requiring bathymetry smoothing, which improves model accuracy at steep bathymetric slopes and sites of complex 3D bathymetry (Yu et al., 2017; Ye et al., 2018).

SCHISM solves the Reynolds-averaged Navier–Stokes equations in hydrostatic and Boussinesq approximated form with a semi-implicit finite-element/finite-volume method and an Eulerian–Lagrangian method (ELM) for momentum advection. The transport equations are solved with a robust third-order Weighted Essentially Non-Oscillatory (WENO) solver in the horizontal and an implicit Total Variation Diminishing (TVD) scheme in the vertical dimension. The advanced transport schemes are crucial for the simulation of baroclinic circulation and mesoscale dynamics in cross-scale applications (Ye et al., 2019). Density is calculated with the non-linear International Equation of State for Seawater (Fofonoff and Millard, 1983). Exchange with the atmosphere is computed with a bulk aerodynamic model (Zeng et al., 1998). Bottom drag is parameterized with the log law drag formula by Blumberg and Mellor (1987) and the use of a constant bottom roughness of 0.5 mm in this study. More detailed descriptions of the SCHISM model are given in Zhang et al. (2016a) and Zhang et al. (2016b).

Turbulence in form of eddy viscosities and eddy diffusivities is computed in SCHISM using the Generic Length-Scale formulation (GLS; Umlauf and Burchard, 2003). The specific parameterization

of the GLS turbulence closure is set according to the k–kl model with KC94 stability functions (Kantha and Clayson, 1994). In this parameterization, the critical gradient Richardson number is Ri_C = 0.25, in accordance with linear stability theory. The background diffusivity is set to 10^{-6} $m^2 s^{-1}$. The maximum cutoff eddy diffusivity is set to 1 $m^2 s^{-1}$.

SCHISM further adds bi-harmonic viscosity to the horizontal momentum equation to effectively remove spurious modes (Zhang et al., 2016b). The domain simulated in this study covers the deep ocean (e.g., eddying regime) and steep bathymetry at the shelf break that particularly exacerbates spurious modes (Yu et al., 2017; Ye et al., 2020). SCHISM augments the dissipation for such conditions by an additional Laplacian viscosity in the form of a spatially variable Shapiro filter (Zhang et al., 2016b; Ye et al., 2020). The local strength of the Shapiro filter is derived as a function of the local bathymetric slope α given by $\gamma = 0.5 \tanh(2\alpha/\alpha_0)$ with a reference slope of $\alpha_0 = 0.5$.

2.2 Ecosystem model ECOSMO

SCHISM is coupled to the biogeochemical model ECOSMO II (Daewel and Schrum, 2013) via the FABM framework (Bruggeman and Bolding, 2014). ECOSMO II is a further developed version of the ecosystem model ECOSMO first introduced for the North Sea (Schrum et al., 2006). ECOSMO II uses a nutrient–phytoplankton–zooplankton–detritus (NPZD) conceptual model approach, and its extended formulation allows the simulation of lower trophic- level dynamics in a wide range of ecosystems (Daewel and Schrum, 2013; Pein et al., 2021; Yumruktepe et al., 2022).

ECOSMO II solves prognostic equations for a total number of 16 state variables. It simulates three separate nutrient cycles for nitrogen, phosphorous, and silicate. Oxygen is solved as an additional tracer. Primary production in ECOSMO II is divided into three phytoplankton functional groups (diatoms, flagellates, and cyanobacteria) and is limited by either nutrients or light. ECOSMO further includes two zooplankton functional groups (herbivorous and omnivorous) and three functional groups for detritus (particulate organic matter, dissolved organic matter, biogenic opal). Benthic–pelagic coupling is considered, as described in Daewel and Schrum (2013). The model considers three different integrated surface sediment pools for each of the three nutrient cycles, one for opal, one for particular organic material consisting of N and C at a Redfield ratio, and one for iron-bound phosphorous. Sediment processes include sediment nutrient release as well as sinking, deposition, and resuspension of POM depending on a critical bottom shear stress.

Light attenuation in ECOSMO II includes phytoplankton self-shading as well as shading by particulate organic matter (POM) and dissolved organic matter (DOM), as proposed by Nissen (2014) and implemented in Zhao et al. (2019). With this dynamical coupling of turbidity to the seasonal primary production cycle, the model explicitly resolves the competing major bottom-up tidal processes controlling primary production, namely, the reduction of light availability by resuspension and mixing of organic matter into the euphotic zone and the supply of nutrients by tidal mixing.

A detailed description of the ecosystem model as well as a validation against observations are given in Daewel and Schrum (2013). The parameter set used in this study is documented in the Supplementary Material (Table S1).

2.3 Model configurations and experiments

The unstructured horizontal grid for the North-West European Shelf-Internal Tide (NWES-IT) model configuration used in this study was constructed with the Surface-water Modeling System software (SMS; Aquaveo, 2019). The NWES-IT domain spans 40°N – 66°N and 20°W – 30°E and thus covers the entire NWES and a part of the northeast Atlantic (see Figure 1). The Baltic Sea is included to adequately resolve basin-exchange processes but is not particularly attended to in this study as it does not feature relevant tidal energy. Sea ice, which usually develops seasonally in the Baltic Sea, is neglected for this study.

SCHISM's cross-scale capabilities are used to achieve telescoping high horizontal resolution in regions affected by internal tide generation at the shelf break and at other extreme bathymetric slopes. The high horizontal resolution of 1.5 km is realized throughout the Celtic Sea and Armorican Shelves and in a 75-km- wide band delimited in an off-shelf direction by the 200-m isobath. The on-shelf extent of 75 km was chosen against the backdrop that most internal tide energy is dissipated within tens of kilometers of their generation site (Pingree et al., 1986; Inall et al., 2011). The horizontal resolution of 1.5 km resolves internal tides with wave lengths of 12–25 km generated by the regionally dominant M2 tide (Guihou et al., 2018). In order to accommodate numerical constraints on model accuracy, the horizontal resolution in the rest of the model domain is determined relative to local water depth and the model time step of 100 s used in this study. This yields a horizontal resolution that smoothly varies from a minimum of ~2.5 km in the shallow coastal zones, or even 500 m at finely resolved areas like the Danish Straits, to a maximum resolution of ~10 km in the deepest parts of the shelf (see Figure 1B). At the shelf break, defined as the 200-m isobath, horizontal grid size smoothly transitions from 1.5 km to a quasi-uniform horizontal resolution of 10 km in the open Atlantic. The NWES-IT horizontal grid comprises a total number of ~386k grid nodes and ~758k triangular grid elements. A model configuration with a uniform horizontal resolution of 1.5 km would require approximately 2.3 million grid nodes. The coupled SCHISM–ECOSMO NWES-IT configuration runs ~170 times faster than real time with 36 CPUs on the Levante HPC-System at the German Climate Computing Center (DKRZ; https://www.dkrz.de, last accessed March 2023).

The coastline for the unstructured horizontal grid was derived from the GSHHS shoreline database at 5-km resolution (Wessel and Smith, 1996). The bathymetry for the domain was interpolated from the EMODnet Digital Bathymetry Digital Terrain Model (version 2018) dataset derived from the EMODnet Bathymetry portal (http://www.emodnet-bathymetry.eu; accessed 04/2020). The bathymetry in the model domain is documented in Figure 1A. The minimum water depth in the domain was set to 10 m to reduce

computational demand. The bathymetry was modified at deep fjords along the Norwegian coast to simplify the horizontal and vertical gridding processes. No other bathymetry smoothing was applied.

The LSC² vertical grid designed for the NWES-IT model configuration realizes a high vertical resolution of 2.5–6 m from the surface to ~60-m depth in order to highly resolve the regional thermocline. The number of layers in the vertical grid varies from three layers for the minimum depth of 10 m to 53 layers for water depths larger than 6,000 m.

Model forcing for temperature and salinity, and ECOSMO state variables nitrate, phosphate, silicate, and oxygen, is provided from WOA2018 climatological data (Boyer et al., 2018). Open boundary conditions for the remaining ECOSMO state variables are taken from a HYCOM–ECOSMO hindcast simulation of the North Atlantic (Samuelsen et al., 2022). Dynamic oceanic forcing is provided twofold. Subtidal SSH and horizontal velocities are provided using daily averages from Samuelsen et al. (2022). The harmonic tidal signal is added to both SSH and the horizontal velocities from the FES2014 product (Lyard et al., 2021) for 15 tidal constituents (Q1, O1, P1, S1, K1, 2N2, MU2, N2, NU2, M2, L2, T2, S2, K2, M4). Corrections for multiyear tidal cycles like the lunar nodal and lunar perigee tide are applied. Tidal potential is applied for the partial tides in the model domain; the effects of self-attraction and loading are neglected. We provide daily river forcing in form of river discharge and nutrient loads for the 172 largest rivers in the domain. River discharge and nitrate, ammonium, phosphate, and silicate loads represent daily mean climatological values computed for the period 1986–2015 from a regional river dataset compiled and used by Daewel and Schrum (2013) and further updated as described by Zhao et al. (2019). We assume ambient temperatures for river discharge. At the sea surface, boundary conditions are provided from a hindcast simulation with the regional atmospheric model COSMO-CLM version 5 with 0.11° horizontal resolution (Geyer, 2017). The atmospheric forcing is provided at an hourly time step. A domain wide bias correction of +15% is applied to shortwave radiation in COSMO-CLM to account for a domain- wide sea surface temperature (SST) bias. Surface albedo is globally set to 0.06, and SCHISM light attenuation parameters are set to Jerlov type IA.

A faster coarse resolution SCHISM–ECOSMO NWES-LR configuration was used to run a 10 year spin-up simulation from which the initial conditions for the NWES-IT configuration are interpolated. The separate coarser resolution NWES-LR configuration was co-developed in the same manner as the NWES-IT configuration. Horizontal- grid resolution in the NWES-LR configuration ranges from 4.5 km in shallow coastal regions to approximately 10 km in deep central shelf areas and reaches 15 km in the open ocean (Supplementary Material Figure S1). The LSC² vertical grid in NWES-LR is the equivalent of the one used in NWES-IT. Temperature, salinity, nitrate, phosphate, silicate, and oxygen for the NWES-LR configuration were initialized from WOA2018 (Boyer et al., 2018). ECOSMO sediment fields for NWES-LR were interpolated from long-term ECOSMO simulations provided by F. Werner (in prep.) and Samuelsen et al. (2022). Forcing data for the spin-up simulations is equivalent to the NWES-IT configuration.

We perform two numerical experiments with the NWES-IT model configuration to assess the impact of tides on NWES primary production. The TIDE experiment includes tidal forcing at the lateral open boundaries and tidal potential in the domain. In the NOTIDE experiment, the same model configuration is run completely without tidal forcing. Both experiments are integrated for a period of 6 years from 2010 to 2015 with hourly instantaneous model output. Model output is averaged to daily means and only saved in full temporal resolution for specified months to reduce memory use. The first year of the TIDE/NOTIDE experiments is treated as a secondary spin-up period and omitted from the analysis.

2.4 Analysis methods for the internal tide field and turbulent mixing

Seasonal stratification on the NWES leads to a quasi two-layer system in spring and summer, with a warm wind-mixed surface layer formed over cold deeper water masses. The pycnocline separates the two layers. Internal tides propagate in the horizontal direction along the pycnocline. In order to achieve realistic bulk mixing, the model needs to adequately represent the properties of the surface and bottom layers, as well as the depth of the layer interface.

We use the potential energy anomaly (PEA, Simpson et al., 1981) to characterize the stratification of the water column. The potential energy anomaly is a measure of the amount of work required to vertically mix the entire water column and is calculated as:

$$\frac{1}{D}\int_{-H}^{\eta} gz(\bar{\rho}-\rho)dz \tag{1}$$

with the depth mean density $\bar{\rho} = \frac{1}{H}\int_{-H}^{\eta}\rho\ dz$, the mean water depth H, the sea surface elevation η, the actual water depth $D = h + \eta$, and the gravitational acceleration g.

In order to assess stratification in vertical temperature profiles, we define the thermocline depth following Guihou et al. (2018) as a normalized first moment of stratification:

$$\delta(t) = H\frac{T_{bed}(t) - \bar{T}(t)}{T_{top}(t) - T_{bed}(t)} \tag{2}$$

Here, H is the depth of the water column, T_{top} and $T_{bed}(t)$ are the surface and bed temperatures at a given time, and $\bar{T}(t)$ is the depth-averaged temperature. The thermocline depth is represented by $\delta(t)$ in the limit of a two-layer vertical density structure. The pycnocline depth is derived in the same manner using density instead of temperature.

Internal waves that propagate along the layer interface lead to oscillatory vertical displacements of the pycnocline. We analyze the variability due to tidally generated internal waves with the help of the tidally filtered interface depth $\langle\,\delta\,\rangle$ computed with a Doodson X0 filter (Intergovernmental Oceanographic Commission, 1985). The pycnocline depth variability is then defined as:

$$\tilde{\delta} = \delta - \langle \delta \rangle . \quad (3)$$

The standard deviation of the tidal fluctuations in pycnocline depth can then be calculated as an estimate of the internal tide activity on shelf scale:

$$std\left(\tilde{\delta}(t)\right) = \sqrt{\frac{1}{72} \sum_{t-36h}^{t+36h} (\tilde{\delta}(t) - \frac{1}{72} \sum_{t-36h}^{t+36h} \tilde{\delta}(t))^2} \quad (4)$$

The standard deviation of $\tilde{\delta}$ is calculated over a moving 3 × 24-h window to avoid aliasing from the spring-neap cycle while retaining sufficient data to isolate a clear signal. The standard deviation of $\tilde{\delta}$ represents a conservative estimate of the tidal variability in the vertical pycnocline displacements (Guihou et al., 2018).

Dissipation of the energy of baroclinic and barotropic tides induces turbulence that mixes nutrients and other tracers in the water column. To assess the ecosystem-relevant turbulent mixing associated with tides, we compute the turbulent nitrate flux in the water column following Sharples et al. (2001) as:

$$J_{NO3} = -K_V(\frac{\Delta NO3}{\Delta z}), \quad (5)$$

with the (vertical) eddy diffusivity K_V computed by the model turbulence closure, the difference in nitrate concentration between the respective discretized vertical model layers $\Delta NO3$, and the vertical model layer thickness Δz in meters. The turbulent nitrate flux J_{NO3} can be used to estimate the potential for new production (Dugdale and Goering, 1967) fueled by allochthonous nitrate from the bottom layer. Assuming full utilization of the vertically mixed nitrate by phytoplankton, we compute potential new production as:

$$PNP = J_{NO3}(z_E) R_N M_C, \quad (6)$$

where $J_{NO3}(z_E)$ is the turbulent nitrate flux evaluated at the base of the euphotic zone, R_N is the standard N:C Redfield ratio, and M_C is the molar mass of carbon.

2.5 Model validation

We evaluate the newly developed NWES-IT configuration's ability to reproduce general hydrographic and biogeochemical conditions on the NWES and specifically assess its skill in regard to tidal processes. We evaluate the results of the TIDE experiment on the western part of the NWES (i.e., the Celtic Seas and greater North Sea) over the 5-year period from 2011 to 2015.

To facilitate model validation, we divide the NWES into subareas (see Figure 1A) following a combination of bathymetric, geographic, and physical and ecosystem considerations based on Holt et al. (2012) and the ICES subareas (ICES, 1983). The greater North Sea is divided into the southern North Sea (SNS), the central North Sea (CNS), the northern North Sea (NNS), the English Channel (EC), the Norwegian Trench (NT), and the Kattegat/Skagerrak (SK) subareas. The Celtic Seas are divided into the Armorican Shelf (A), the Celtic Sea (C), the Irish Sea (I), the Inner Seas off the West Coast of Scotland (Sc), and the North-Western Approaches (NWA). The Celtic Sea and the North-Western Approaches are further separated into smaller subareas for a more detailed analysis of tidal impacts. The northeastern inner shelf region (NEC) and the southwestern outer shelf region (SWC) of the Celtic Sea are separated by the approximate 130-m isobath. The North-Western Approaches subarea is divided into the Western Irish Shelf (WI), the Malin Shelf (MS), and the Hebrides Shelf (HS).

2.5.1 Tides

The NWES-IT model configuration´s ability to simulate barotropic tides is evaluated against observational data from tide gauges and tidal current meters. Tide gauge data are compiled from CMEMS *In Situ* TAC (http://www.marineinsitu.eu; last accessed 08/2022), UHSLC tide gauge data (Caldwell et al., 2015), and the UK Tide Gauge Network provided by the British Oceanographic Data Centre (https://www.bodc.ac.uk/data/hosted_data_systems/sea_level/uk_tide_gauge_network; last accessed 08/2022). Simulated tidal currents are compared against observational data from the British Oceanographic Data Centre (made available by Karen Guihou under a CECILL license at https://github.com/Karen-Guihou/tidal_analysis; last accessed 08/2022).

Hourly model output from the TIDE experiment in July and August 2014 is used for the harmonic analysis of the tidal signal. Statistics are computed for the eight major constituents and shown in Table 1. For the regionally dominant M2 constituent, tidal elevations yield an RMSE of 33.15 cm and a mean error of −7.33 cm. The RMSE for the maximum M2 tidal current velocities is 13.42 cm/s, with a mean error of 3.5 cm/s. Mean errors in both tidal elevations and maximum tidal current velocities of the regionally dominant M2 constituent compare well with the performance of established NEMO AMM7 configurations (O'Dea et al., 2012; Guihou et al., 2018). RMSE for the M2 constituent in the SCHISM NWES-IT configuration is somewhat higher than in NEMO AMM7, which might be related to model boundary forcing and the implemented 10-m minimum water depth. Overall, Table 1 documents generally good comparability between model and observations and underlines adequate model performance in regard to tides.

2.5.2 General hydrography

We assess the adequate representation of the spatial, seasonal, and interannual variability of temperature by co-locating observation and model data in space and time against *in situ* temperature data obtained for the period 2011–2015 from the ICES database (https://data.ices.dk; downloaded 12/2022). The ICES data comprises a total number of 17,420 temperature profiles from CTD casts. Each CTD cask is depth-averaged for comparison against model data to account for differing vertical discretization. The Taylor diagram shown in Figure 2A demonstrates a good fit between the model and observational data for the defined subareas. Centered RMSE (CRMSE) errors are low (≤ 0.5), and the correlation between model and observational data is high (R >0.85) except for the Norwegian Trench area (excluded in Figure 2A). The mean temperature bias calculated for the co-located data included in the Supplementary Material (Table S2) further underlines the good model performance.

TABLE 1 RMSE and mean error for comparison (model-obs) of model results against harmonic analysis from tide gauge data and tidal current semi-major axis from historical current meter data for the NWES.

Constituent	Elevation [cm]			Current [cm/s]		
	RMSE	Mean error	N	RMSE	Mean error	N
Q1	1.67	-0.47	120	–	–	–
O1	1.88	-0.17	120	0.91	-0.04	269
K1	2.77	+0.45	120	0.99	-0.05	269
N2	6.86	+2.33	c120	3.93	+2.33	261
M2	33.15	-7.33	120	13.42	+3.05	270
S2	14.48	-4.5	120	4.95	+2.01	272
M4	5.04	1.63	120	1.23	-0.55	262

Harmonic analysis is computed from hourly model data for July and August 2014. Outliers are removed (>2.58 STD), N shows number of valid data used in the comparison.

We further compare mean summer (JJA) sea surface temperatures (2011–2015) against satellite observations obtained from the European Space Agency SST Climate Change Initiative (ESA SST CCI) reprocessed sea surface temperature analysis (https://doi.org/10.48670/moi-00169; downloaded 11/2022). Figure 3A shows simulated mean summer SST for 2011–2015. SST on the NWES has a latitudinal gradient. It is highest in the Celtic Sea (16°C–18°C), followed by the shallow southern North Sea (15°C–17°C). Surface temperature then decreases with latitude and reaches temperatures around 12°C in the northern North Sea. The model configuration reproduces a cool band of summer SST with a distinct difference of 1°C – 2°C to adjacent areas along the shelf break of the Armorican and Celtic Sea. Such a band of cold SST is frequently documented in observations (Pingree et al., 1982; Sharples et al., 2007). Comparison with the observed SST field from ESA SST CCI satellite data in Figure 3B shows high agreement between the two fields. The mean bias is below ± 0.5°C in most of the domain. Too warm temperatures along the Celtic Sea shelf break suggest underestimated mixing in the region, and too cold temperatures along the northwestern GB coast conversely suggests minor overmixing.

Stratification is evaluated by a direct comparison of vertical temperature structure against observations from a mooring station in the Celtic Sea. Data for the CSE5 mooring station in the Celtic Sea was obtained from the UK FASTnet project (https://www.bodc.ac.uk/projects/data_management/uk/fastnet, downloaded 08/2022). The CSE5 mooring station was deployed at a distance of approximately 40 km to the Celtic Sea shelf break in a mean water depth of 184 m. The nominal position of the CS5 station is 48.77° N and 9.41° W. The CSE5 station is marked in Figure 1B. The water column at the CSE5 station shown in Figure 4 features a well-established two-layer system in June 2012. Simulated temperatures of 13.5°C–15°C in the surface mixed layer match observations, and the model resolves the cooling of the surface layer during a wind event on 14–18 June. The

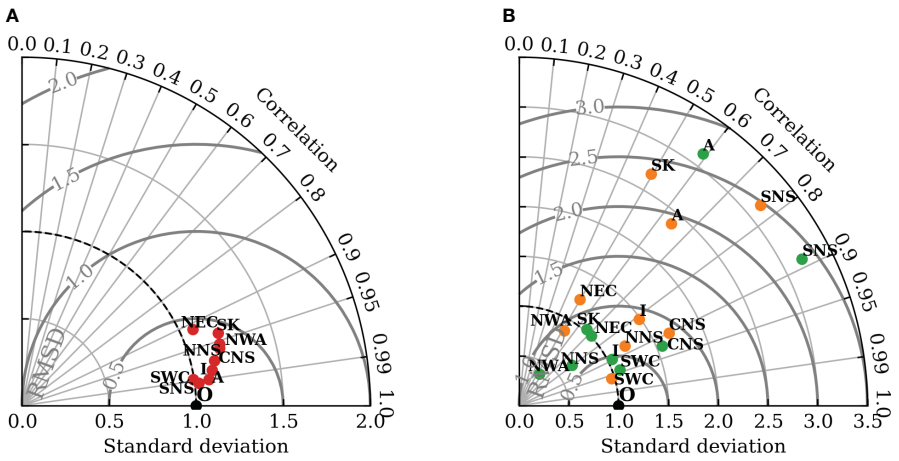

FIGURE 2
(A) Taylor diagram of depth-averaged model temperature co-located against observational data (2011–2015) downloaded from the ICES database (https://data.ices.dk; downloaded December 2022). Data are co-located in time and space for a total number of 17,420 temperature profiles from CTD casts. **(B)** Taylor diagram for surface (<20 m) nitrate (orange) and phosphate (green) concentrations co-located to ICES observational data (2011–2015). We use a total number of 6,045 stations for nitrate and 6,083 stations for phosphate.

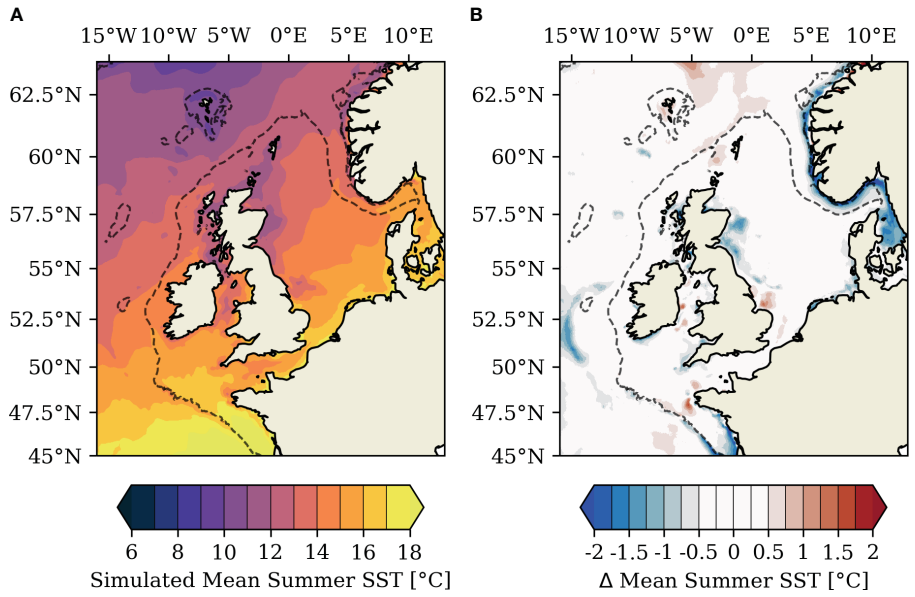

FIGURE 3
Simulated mean summer (JJA) SST for 2011–2015 **(A)** and temperature bias for simulated mean summer SST (2011–2015) against ESA SST CCI satellite observations **(B)**.

thermocline depth is captured well in the model. Bottom temperatures at the CSE5 station are marginally overestimated by 0.25°C–0.5°C in the model.

The presented validation of temperature indicates an overall good representation of the spatial, seasonal, and interannual variability of temperature and the associated mixing-stratification status on the shelf. An additional comparison of mean sea surface salinity to climatological data from the Baltic and North Seas climatology (BNSC; Hinrichs and Gouretski, 2019) is included in the Supplementary Material (Figure S2). The model configuration enables the efficient simulation of the general hydrography of the NWES required to capture relevant coupled physical–biogeochemical circulation features (Pätsch et al., 2017).

2.5.3 Internal tides

The vertical temperature profile in Figure 4 shows high-frequency oscillatory vertical displacements of the thermocline also documented in observations. Such thermocline depth variability indicates the presence of internal tides. We use the

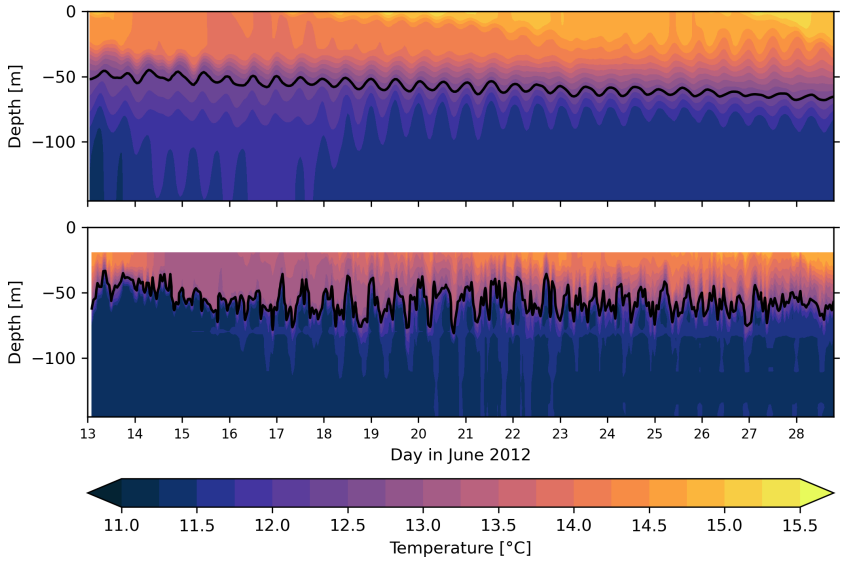

FIGURE 4
Time series of temperature at the CS5 station at 48.77°N, 9.4°W from model (top) and observations (bottom). Black contour indicates thermocline depth computed with Eq. 2.

tidal thermocline depth variability defined in Eq. 3 to evaluate the model's ability to reproduce internal tides in more detail. We extract the tidal thermocline depth variability at the CS5 station as well as at the CCS, MSE, and HSE stations on the NWES (all stations are marked in Figure 1B). The CS5 station features low-mode internal tides but is positioned well out of the complex internal tide generation zone at the shelf break (Hopkins et al., 2014). The CCS station is located in the central Celtic Sea at a nominal position of 49.32° N and 8.49°W with a mean water depth of 145.4 m. Observational data at the CCS station are available for August 2014 from the UK Shelf Sea Biogeochemistry project (Wihsgott et al., 2016). The MSE station is located at the shelf break of the Malin Shelf at 55.87° N and 9.06° W with a mean water depth of 149 m. The HSE station is positioned at 58.7°N and 7.6°W in proximity of the shelf break of the Hebrides shelf and has a mean water depth of 153 m.

At the CCS and CS5 stations, we extract the tidal thermocline depth variability for the respective observational periods to allow evaluation against observations. At the MSE and HSE stations, we extract data in August 2014 to evaluate stratified conditions. The fast Fourier transform spectral (FFT) analysis of the thermocline depth signal in Figure 5 shows that the thermocline depth variability at all stations clearly shows frequency banding that is best captured by regionally relevant M2, M4, and S1 tidal harmonic bands. The frequency banding fits well with observations at the CS5 and CCS stations. The M2 frequency band holds the most energy at all four stations. The model underestimates the energy in the M2 tidal frequency band at the CS5 station close to the shelf break. The simulated energy in the M2 frequency band fits with observations at the CCS station in the central Celtic Sea. The model further generally underestimates energy in higher frequency bands, e.g., for the M4 and M6 overtides, at both the CS5 and CCS stations.

2.5.4 Biogeochemistry

We assess the model's consistency with large-scale nutrient distributions and seasonality against *in situ* data of nutrients obtained from the ICES database (https://data.ices.dk; downloaded 11/2022) for the period 2011–2015. Similar to Daewel and Schrum (2013), we compute the vertical integral of the observational data in the top 20 m if observations at different depth levels are available. For stations with surface values only (max. depth< 5m), we use the shallowest observation for direct co-location, as the thickness of the surface layer in the model ranges between 2.5 and 5 m. The observational data is co-located in time and space against daily mean model output of the TIDE experiment, and we visualize the normalized statistics for the different subareas with the help of a Taylor diagram in Figure 2B.

For nitrate, the Taylor diagram in Figure 2B shows centered RMSE values < 1 for all subareas except the Armorican shelf (CRMSE ≈ 1.9), the Skagerrak/Kattegat region (CRMSE ≈ 2.4), the southern North Sea (CRMSE ≈ 2.5), and the northeastern Celtic Sea (CRMSE ≈ 1.2). Normalized standard deviation is slightly below 1 for the NWA and SWC subareas and between 1 and 1.75 for NEC, I, NNS, and CNS subareas, indicating a slightly underestimated/overestimated representation of nitrate variability in the respective subareas. The SNS, A, and SK subareas have high standard deviation (> 2). The correlation is > 0.5 for all subareas except SK (≈ 0.49). The correlation is > 0.8 for the CNS, NNS, and SWC subareas.

Model performance for phosphate is slightly better than for nitrate (Figure 2B) but also shows reduced performance for the A and SNS subareas. Centered RMSE is high for the southern North Sea and Armorican Shelf but < 1 for the other subareas. The standard deviation shows a pattern similar to CRMSE; it is high for the SNS and A subareas, intermediate for the CNS (≈ 1.6), and around 1 for SK, NEC, SWC, and I. The standard deviation is < 1 for NNS and NWA. The correlation is higher than for nitrate, with all subareas showing correlation > 0.6 except for the NWA (≈ 0.54) and A subareas (≈ 0.59). The correlation is particularly high (>0.8) for SWC, I, SNS, and CNS subareas.

We complement the normalized and centered statistics with the percentage bias (Allen et al., 2007) documented in Table S2 in the Supplementary Material. The percentage bias shows decent model performance on the NWES but again shows a reduced model skill particularly in shallow subareas like the southern North Sea, northeastern Celtic Sea, or the Irish Sea. The model's particular difficulties in reproducing low summer nutrient concentrations in shallow regions is a common issue with ECOSMO. Daewel and Schrum (2013) relate the reduced model skill in shallow coastal regions to unconsidered impacts of near-coast ecosystems (e.g., the Wadden Sea) and the utilization of Redfield stoichiometry in the model. Other aspects of the presented nutrient validation, like

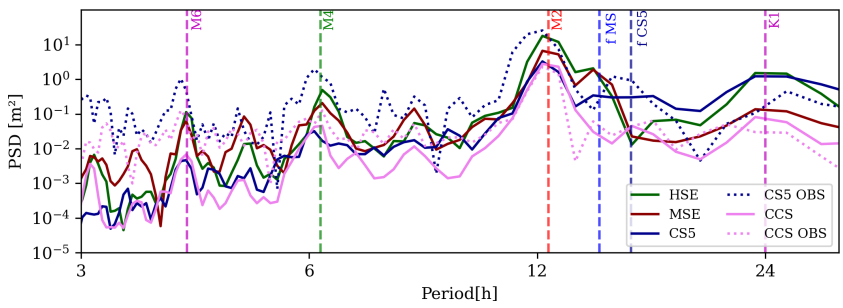

FIGURE 5
Frequency analysis of thermocline depth signal at CCS, CS5, MSE, and HSE stations. The FFT is implemented with a Welch filter (with 192h segments) and a Hanning window (with 50% overlap). Dotted lines show frequency analysis of available observational data.

thebetter model performance in regard to phosphate, show promising consistency with previous model studies based on smaller domain sizes and different physical model components (Daewel and Schrum, 2013; Zhao et al., 2019).

Mean annual primary production in the TIDE experiment (2011–2015) shown in Figure 6A reproduces the characteristic spatial pattern of primary production on the NWES (e.g., Holt et al., 2012; Holt et al., 2016). Shallow and coastal regions feature high primary production, whereas NPP is substantially lower in the deeper central basins of the shelf where seasonal stratification limits vertical nutrient supply. NPP simulated with ECOSMO is typically in the lower range of what is reported in literature for the region (Daewel and Schrum, 2013; Zhao et al., 2019). Productivity is particularly low along the European continental coast, where observations suggest NPP to range from 199 to 261 $gCm^{-2}yr^{-1}$ (Joint and Pomroy, 1993). Simulated annual NPP of 70–85 $gCm^{-2}yr^{-1}$ in the stratified central Celtic Sea fits well with published estimates of 80 $gCm^{-2}yr^{-1}$ based on *in situ* incubations (Joint and Groom, 2000). The model also resolves intensified biological productivity in tidal frontal zones (Mann and Lazier, 2013), e.g., in the southern North Sea, along the western British coast, the English Channel, or between the Irish and Celtic Seas. A qualitative comparison of mean seasonal phytoplankton biomass to a chlorophyll-a Copernicus Global Colour satellite product (https://doi.org/10.48670/moi-00281, downloaded 5/2023) in Figure S3 shows the adequate seasonal evolution of phytoplankton biomass in the model. The model reproduces a pronounced bloom in spring and subsequent bloom progression from south to north in summer also documented in the satellite chlorophyll-a product. Phytoplankton biomass and chlorophyll-a are high in the shallow coastal areas throughout the summer, whereas the seasonally stratified central basins of the North Sea and Celtic Sea show low values due to nutrient limitation in the surface layer in summer.

Light attenuation in ECOSMO II explicitly includes phytoplankton self-shading as well as shading by POM and DOM. In combination with resolved benthic–pelagic coupling by sedimentation and resuspension of POM, this allows the representation of the spatially diverse primary production dynamics in turbid coastal regions of the NWES (Capuzzo et al., 2013; van Leeuwen et al., 2015; Taylor et al., 2021). Figure S4 shows a qualitative comparison of simulated mean seasonal surface organic detrital matter concentration (DOM + POM) with the volume absorption coefficient of radiative flux in sea water due to dissolved organic matter and other detrital organic particles obtained from a Copernicus Global Colour satellite product (https://doi.org/10.48670/moi-00281, downloaded 5/2023). Figure

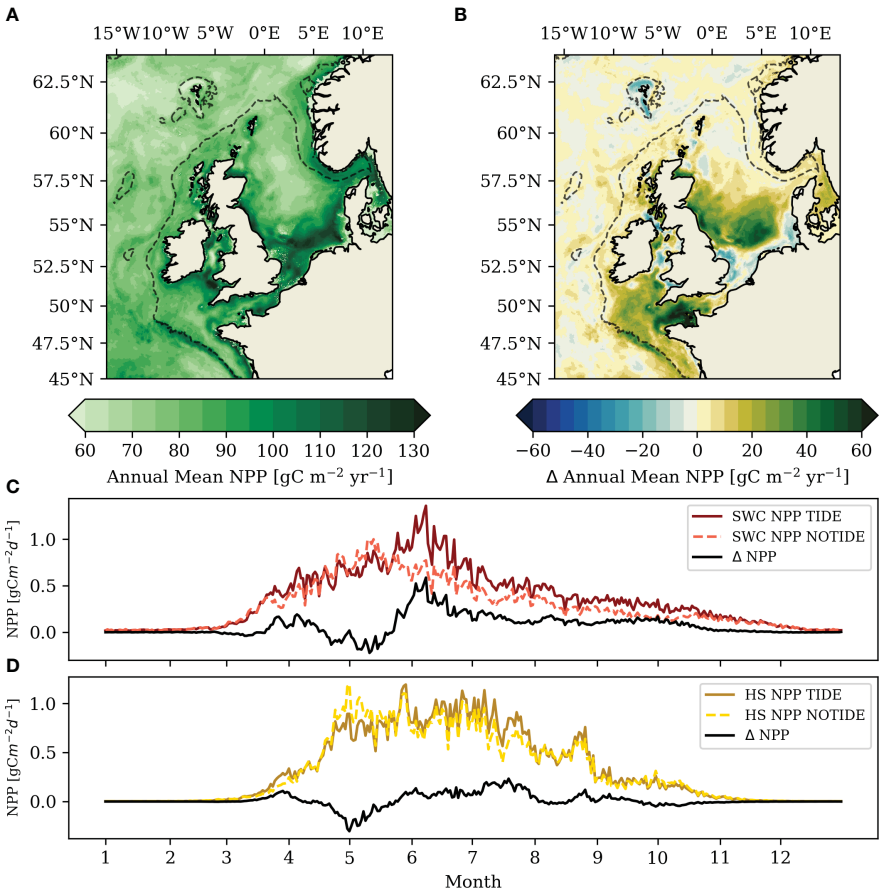

FIGURE 6
(A) Mean annual primary production (2011–2015) in TIDE experiment and **(B)** difference in mean annual primary production for 2011–2015 between the experiments (TIDE–NOTIDE). Dashed black contour shows the 200-m isobath. Daily primary production computed for period 2011–2015 for the southwestern Celtic Sea **(C)** and Hebrides Shelf subareas **(D)**.

S4 documents the adequate spatial distribution of DOM and POM in the model. Maximum DOM and POM concentrations and associated light absorption occur in the shallow near-coast areas, especially in permanently mixed regions with strong resuspension of POM. The seasonality of DOM and POM varies with the seasonal cycle of primary productivity, which is also present in the satellite-derived absorption coefficient.

The consistency across model configurations and the overall good agreement between simulated nutrient fields and ICES observation data affirm overall adequate SCHISM–ECOSMO performance in regard to simulated biogeochemical cycles. SCHISM–ECOSMO resolves key processes regarding the effects of tidal forcing on nutrients and light, and the presented validation analysis encourages the use of SCHISM–ECOSMO for the investigation of tidal impacts on primary production on the entire shelf.

3 Results and discussion

3.1 Tidal mixing and the internal tide field in the NWES-IT model configuration

The signature of tidal mixing is illustrated in Figure 7A by means of the annual mean Potential Energy Anomaly (PEA; Eq. 1) computed for the period of maximum stratification from mid-June to mid-August (2011–2015). Permanently mixed areas (PEA < 20 Jm^{-3}) are separated from seasonally stratified areas by tidal mixing fronts, e.g., in the southern North Sea, the western approaches of the English Channel or the St. George front separating the Celtic and Irish Seas. PEA magnitude and the positions of the tidal fronts match results of previous studies and observations (Holt and Umlauf, 2008; Pätsch et al., 2017; Graham et al., 2018a) and thus further substantiate the adequate simulation of the mixing-stratification status on the NWES outlined in Sect. 2.5.

The refined horizontal grid resolution in the NWES-IT configuration reproduces pycnocline depth variability at tidal frequencies that suggests the presence of kilometrical-scale internal tides (Sect. 2.5.3). We compute the pycnocline depth tidal standard deviation $std(\tilde{\delta})$ (Eq. 4) for a spring tide period from 11 to 14 August 2014 to evaluate the resolved internal tide activity on the entire NWES. We chose a period in early August because the vertical temperature gradients, which mainly control stratification on the NWES, are largest in late July and early August.

The computed $std(\tilde{\delta})$ in Figure 7B shows high spatial variability on the NWES; it ranges from 0 to over 8 m at sites along the shelf break. The results from the NWES-IT configuration show high consistency with kilometrical-scale regional model results presented by Guihou et al. (2018). The $std(\tilde{\delta})$ along the shelf break of the northern North Sea, where the continental slope is subcritical for internal tide generation (Huthnance et al., 2022), is low. The local horizontal grid resolution (6–10 km; see Figure 1B) does not resolve kilometrical-scale processes in the central North Sea, and the NWES-IT configuration consequently does not reproduce internal tides in this region. The study of Guihou et al. (2018) shows only very low internal tide activity in the central North Sea, so that the low internal tide activity in the NWES-IT configuration fits with the expected internal tide activity in the region. The $std(\tilde{\delta})$ in Figure 7B is significantly elevated along the steep shelf break of the Celtic Sea, in line with multiple observational studies that show high internal tide activity in this region (Pingree and Mardell, 1985; New and Pingree, 1990; Sharples et al., 2007; Green et al., 2008; Inall et al., 2011). The $std(\tilde{\delta})$

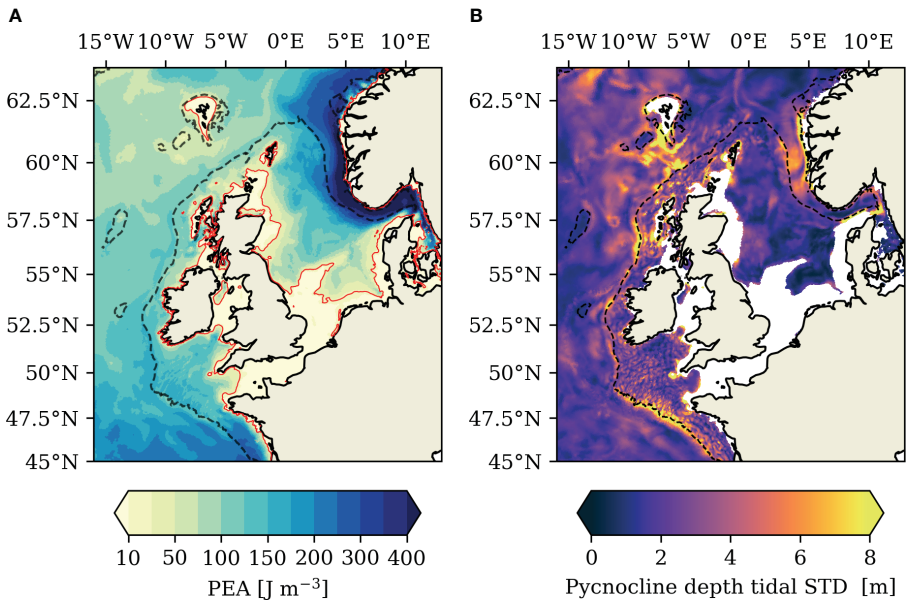

FIGURE 7
Mean Potential Energy Anomaly for period of highest stratification in TIDE experiment (15 July – 15 August; mean for 2011–2015) computed for top 200 m **(A)**. Pycnocline standard deviation in TIDE experiment computed for spring tide period 11 – 14 August 2014 for top 200 m **(B)**. Permanently mixed regions ($PEA < 20\ Jm^{-3}$) are masked out in **(B)**. Please note the non-proportional color bar discretization in **(A)**.

is also elevated on the Malin Shelf and its continental slope, where on-shelf propagation of internal tides has also been observed (Sherwin, 1988; Rippeth and Inall, 2002). The $std(\tilde{\delta})$ is intermediate on the narrow Hebrides Shelf but is elevated on the continental slope close to the Wyville Thomson Ridge known for internal tide generation (Sherwin, 1991; Hall et al., 2019).

The fine-scale structure of $std(\tilde{\delta})$ throughout the Celtic Sea further suggests a complex and spatially variable internal tide field with internal tide generation at small-scale bathymetric features like canyon ridges and sea banks. Increases of $std(\tilde{\delta})$ at the edge of the permanently mixed areas on the shelf do not indicate increased internal tide activity but reflect reduced stratification. The resolved spatial variability of internal tide activity in the Celtic Sea is consistent with the results of Guihou et al. (2018) and non-hydrostatic simulations in smaller areas of the Celtic Sea (Vlasenko et al., 2013; Vlasenko et al., 2014).

3.2 Tidal impacts on primary production on the NWES

We investigate the impact of tidal forcing on primary production on the NWES by comparing the mean annual primary production (2011–2015) from the NWES-IT experiments with and without tidal forcing. Figure 6A shows mean annual net primary production (NPP) in the TIDE experiment with tidal forcing. Figure 6B shows the respective difference in mean annual NPP between the TIDE experiment and the NOTIDE experiment. Table 2 further documents the NPP response to tidal forcing for the subareas introduced in Sect. 2.5. Note that the Celtic Sea and the North-Western Approaches are separated into smaller subareas for a more detailed analysis of tidal impacts, as described in Sect. 2.5.2 and documented in Figure 1B.

The comparison of mean annual NPP in the two experiments in Figure 6B shows that tidal forcing extensively structures biological productivity on the NWES. Tidal forcing substantially increases mean annual primary production on the shelf by around 16% (~14.47 Mt C; Table 2). The tidal response of primary production on the inner shelf found in this study is similar to results obtained by Zhao et al. (2019) for the central and southern North Sea. Tidal impacts on the inner shelf can largely be classified based on stratification characteristics and water depths. Tidal forcing decreases productivity in the majority of the shallow permanently mixed regions of the NWES (see PEA in Figure 7A). The tidal NPP response is also negative in the tidally energetic North Channel between Ireland and the UK. Shallow stratified areas of the NWES in turn are particularly responsive to tidal mixing of nutrients and show strong productivity increases. The dynamic tidal frontal systems in the southern North Sea, northeastern Celtic Sea, or western English Channel particularly invigorate local primary production in the TIDE experiment.

The tidal NPP response is generally lower in the deep outer shelf regions of the NWES. The northern North Sea shows a minor positive response to tidal forcing (+2%; Table 2) but features local reductions of up to -10 $gCm^{-2}yr^{-1}$. Tidal NPP response on the northern North Sea continental slope is neutral or marginally

TABLE 2 Annual mean primary production (2011–2015) on the NWES in NOTIDE and TIDE experiments.

Subarea	NOTIDE	TIDE	Difference
	Total $[Mt\ C\ yr^{-1}]$ (Mean $[gC\ m^2yr^{-1}]$)	Total $[Mt\ C\ yr^{-1}]$ (Mean $[gC\ m^2yr^{-1}]$)	
S. North Sea (SNS)	17.48 (85.7)	19.9 (97.5)	+ 14%
C. North Sea (CNS)	16.44 (67.7)	19.33 (79.6)	+18%
N. North Sea (NNS)	5.89 (74.4)	6.02 (76.0)	+2%
Skag./Kattegat (SK)	5.16 (66.3)	5.77 (74.2)	+12%
Norwegian Trench (NT)	6.44 (82.9)	6.57 (84.6)	+2%
English Channel (EC)	4.82 (58.6)	7.49 (91.1)	+55%
Armorican Shelf (A)	5.36 (76.3)	6.21 (88.4)	+16%
N-E Celtic Sea (NEC)	7.66 (71.4)	9.86 (91.9)	+29%
S-W Celtic Sea (SWC)	6.16 (67.5)	7.69 (84.3)	+25%
Irish Sea (I)	4.04 (84.7)	4.27 (84.5)	+6%
I. Sea W. of Scotl. (Sc)	3.24 (73.3)	3.63 (82.2)	+12%
West Irish Shelf (WI)	3.67 (78.2)	3.89 (82.9)	+6%
Malin Shelf (MS)	1.64 (77.1)	1.74 (81.5)	+6%
Hebrides Shelf (HS)	2.73 (77.4)	2.84 (80.4)	+4%
Sum for NWES	90.74 $Mt\ C\ yr^{-1}$	105.21 $Mt\ C\ yr^{-1}$	+16%

Difference between experiments computed relative to NOTIDE experiment.

negative. Tidal forcing also locally decreases NPP on the Hebrides shelf, but the HS subarea still shows an aggregated increase of +4%. At around 58°N, tidal forcing locally increases NPP by 10 – 15 $gCm^{-2}yr^{-1}$ in a patch on the continental slope. The tidal NPP response further increases southward and yields +6% for the Malin Shelf subarea, where NPP is particularly enhanced by tidal forcing in a small region that also features high internal tide activity in Figure 7B. NPP is also increased by 10 – 15 $gCm^{-2}yr^{-1}$ on the continental slope of the Malin Shelf at around 55.5°N and on the northern flank of the Porcupine Seabank.

The Celtic Sea in the southwest of the NWES stands in stark contrast to the North-Western Approaches, highlighting substantial regional differences in the impact of tidal forcing on primary production along the NWES shelf break. Although the water depth in the southwestern Celtic Sea (SWC) subarea is comparable with, e.g., the NNS (> 130 m), the SWC subarea still shows a substantial NPP increase of +25% with tidal forcing (Table 2). Highest NPP increases (locally up to 50 $gCm^{-2}yr^{-1}$) occur on the continental slope of the Celtic Sea in the English Channel tidal flux window at around 5.5 – 8.5°W. Tidal forcing moreover substantially increases NPP in the deep outer shelf area along the Celtic Sea shelf break (up to 30 $gCm^{-2}yr^{-1}$) and the central Celtic Sea (up to 35 $gCm^{-2}yr^{-1}$). The deep water column limits the impact of the barotropic tide in the region. Figure 7B however indicates high internal tide activity.

We turn to the seasonal cycle of NPP to examine the regional differences of the tidal NPP response in the deep shelf areas along the shelf break in more detail. Figures 6C, D show the mean seasonal cycle of NPP (2011–2015) averaged for the southwestern Celtic Sea (SWC, Figure 6C) and the Hebrides Shelf (HS, Figure 6D) subareas. The seasonal cycle of NPP in the TIDE experiment in Figure 6C fits with observations by Joint et al. (2001), who found an extended spring bloom from March to June in the Chapelle Bank region on the Celtic Sea shelf break. Tidal forcing marginally increases spring NPP in the HS subarea in March and then decreases from April to early June (Figure 6D). In the Celtic Sea, tidal forcing similarly increases NPP in late March/early April and then reduces NPP until late May. The decrease of spring NPP by tidal forcing is more pronounced in the HS subarea than in the SWC subarea. We attribute the reduction in spring NPP to a delay of the spring bloom that is caused by the deepening of the mean spring surface mixed layer in the TIDE experiment by 8 and 4 m in the HS and SWC subareas, respectively. In a deeper mixed layer, phytoplankton spends less time in favorable light conditions close to the surface, which hinders the buildup of spring bloom biomass in this period. This mechanism was also identified for the northern North Sea in Zhao et al. (2019).

Tidal forcing continuously enhances NPP during the summer bloom period in the southwestern Celtic Sea. The largest tidally induced increase in NPP in the SWC occurs in late spring/early summer; the averaged NPP in the SWC is up to 6 $gC\,m^{-2}d^{-1}$ higher in the TIDE experiment in late May/early June. Tidal forcing moreover marginally increases autumn NPP in the SWC. Tidal forcing also increases summer NPP in the HS subarea, but the magnitude of the increase is substantially lower (only up to 2 $gC\,m^{-2}d^{-1}$) than in the SWC. In the HS subarea, the largest difference between the TIDE and NOTIDE experiment occurs in July.

Tinker et al. (2022) have shown significant tidal impacts on the residual circulation on the NWES, which are reproduced in our study (Figure S5 Supplementary Material). Tidal phase-driven transport can locally increase residual shelf circulation. Tides also increase bed friction on the shelf, which in turn can decrease the residual shelf circulation. The latter tidal impact particularly affects regions of freshwater influence (Lin et al., 2022; Tinker et al., 2022). A tidal slowing of river water export may contribute to the decrease in mean (summer) surface nutrient concentrations found in ROFIs along the Dutch and German continental coast or in the English Channel (see Figure 8). The (permanently mixed) near-coast areas however are not nutrient limited but light limited (Tett and Walne, 1995) because of intense vertical mixing, high riverine nutrient inputs, and on-shore transport of nutrients and organic matter by estuarine-type circulation (Hofmeister et al., 2017). The reduction of the residual circulation along the continental coast is thus not the decisive factor for the negative near-coast NPP response to tidal forcing. Instead, in line with Zhao et al. (2019), we find that this impact is caused by the degradation of local light conditions due to tidally enhanced resuspension and vertical mixing of POM. Zhao et al. (2019) further established that the major tidal impact on NPP in the seasonally stratified and tidal frontal regions of the North Sea is *via* vertical mixing of nutrients. We therefore focus our analysis of tidal impacts on vertical mixing in the following sections.

The presented study considers major bottom-up processes controlling the tidal impact on primary production, including the tidal mixing of nutrients and organic matter, as well as the resuspension of POM. The 10-m minimum water depths used in this study however limits the representation of particularly shallow coastal regions, as a wetting and drying scheme is not implemented in the model configuration. River plumes and related near-coastal currents may therefore be underrepresented. Moreover, the identified sensitivity of primary production to tidal forcing could be affected by sediment retention by macrobenthos (Prins et al., 1996; Kamp and Witte, 2005; Le Guitton et al., 2017) and its impact on water column turbidity through reduced POM resuspension. The influence of inorganic suspended particulate matter on tidal impacts on NPP is another source of uncertainty in the presented approach that needs to be addressed in future research.

3.3 Vertical mixing by the barotropic and baroclinic tide

We investigate the tidal impact on vertical mixing of nutrients to evaluate its role for the tidal NPP response shown in the previous section. In light of the substantial positive NPP responses found in areas of internal tide activity, we will particularly evaluate the impact of internal tides on vertical mixing. We focus on nitrate in the following, as it is the main limiting nutrient for primary production in the stratified regions of the NWES. We compute the mean turbulent nitrate flux $\overline{J_{NO3}}$ (Eq. 5) during the period of strongest stratification (15 July– 15 August; mean for 2011–2015) to assess how effective turbulence in the water column mixes across

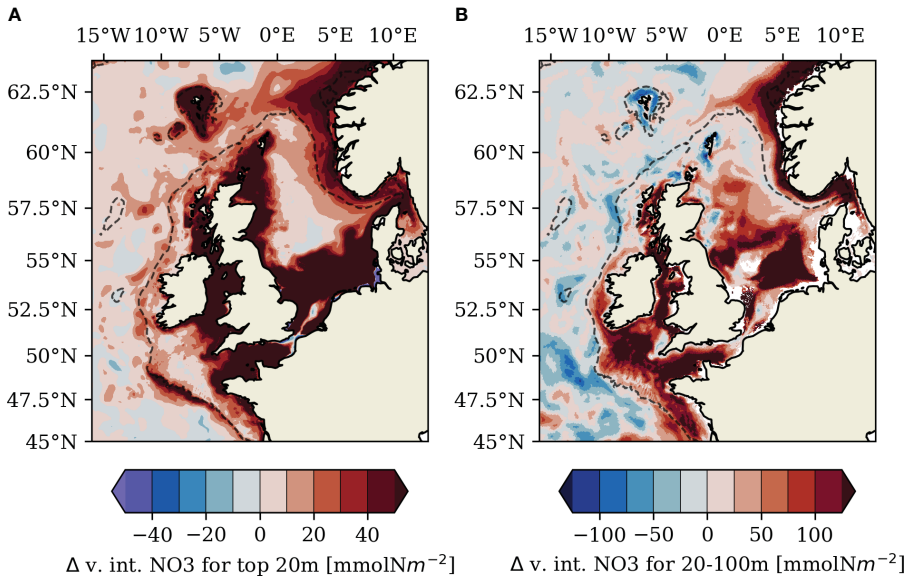

FIGURE 8
Difference (TIDE−NOTIDE) of mean nitrate concentration in June (2011–2015) vertically integrated over **(A)** the surface layer (top 20 m) and **(B)** over internal depths (20–100 m).

the nitrate gradient and replenishes nutrients in the euphotic zone. Figure 9A shows the difference in $\overline{J_{NO3}}$ between the TIDE experiment and the NOTIDE experiment along a vertical transect that spans from the tidal frontal region in the Irish Sea to the shelf break of the Celtic Sea. The transect is marked in Figure 1B. The corresponding vertical transect of mean eddy diffusivity $\overline{K_V}$ from the TIDE experiment is shown in Figure 9B.

In shallow regions with strong tidal currents, like the Irish Sea on the left- hand side of Figure 9, tides and wind generate turbulence in the entire water column (Figure 9B). In transitionary tidal frontal areas, the surface and bottom layer strongly interact and wind forcing or the spring-neap tidal cycle can laterally move the tidal front. The persistent competition between tidal mixing and thermal stratification generates intense turbulent mixing of nutrients into the upper water column on the stratified side of the front (e.g., Pingree et al., 1975). Changes in stratification and/or the vertical nitrate gradient by tidal stirring in the bottom boundary layer can also decrease turbulent transports in some regions (see Figure 9A).

In the stably stratified section of Figure 9, the pycnocline (marked by the N^2 contours) suppresses turbulence and acts as a flux barrier. Tidal forcing can however also generate turbulence within the pycnocline, where turbulence has a particularly high mixing efficiency due to stronger vertical gradients (Rippeth, 2005). Figure 9A accordingly shows high tidally generated $\overline{J_{NO3}}$ at the base of the pycnocline in the northeastern Celtic Sea (water depth< 130m). Pycnocline mixing is elevated at bathymetric features and particularly high at the Jones Bank (approx. 350km in Figure 9).

Pycnocline mixing requires shear to be produced in the pycnocline, either directly by the barotropic tide, internal waves, or wind-induced inertial oscillations. Becherer et al. (2022) found the barotropic tide alone to produce sufficient shear at the base of pycnocline to generate observed diapycnal mixing in the shallow southern North Sea. In the Celtic Sea, with its energetic internal tide field, internal wave breaking will contribute as well. The separation of the surface and boundary mixed layers increases in the deeper water column in the southwestern part of the transect shown in Figure 9 (beyond the Jones Bank). Here, the impact of the barotropic tide becomes negligible and pycnocline mixing relies on shear instabilities produced by inertial oscillations and internal waves. Figure 9A shows tidal forcing enhances $\overline{J_{NO3}}$ within the pycnocline in the deep southwestern section of the transect. Tidal forcing particularly enhances $\overline{J_{NO3}}$ within the pycnocline in the region close at the shelf break. Turbulent mixing of nitrate across the pycnocline has been observed in the shelf regions along the Celtic Sea shelf break and is attributed to mixing by the energetic internal tide field (Sharples et al., 2007; Sharples et al., 2009). Tidally elevated $\overline{J_{NO3}}$ in the pycnocline in proximity to the Jones Bank further suggests mixing by internal tides generated at the local extreme bathymetry, which also fits with observations (Palmer et al., 2013; Tweddle et al., 2013).

3.4 Tide-generated vertical mixing of nutrients across the pycnocline

To obtain a shelf-wide estimate of the turbulent transport that can sustain (new) primary production in the stratified system during summer, we evaluate the mean turbulent nitrate flux at the nutricline (denoted as $\overline{J_{NO3}(z_N)}$ in the following). We define the nutricline as the maximum vertical nitrate gradient in the water column. We here follow Sharples et al. (2001) and utilize the condition that primary production sets up the nutricline at the base of the euphotic zone below the subsurface biomass maximum in the pycnocline. We show $\overline{J_{NO3}(z_N)}$ averaged for the period of maximum stratification from the 15 July to 15 August for the entire

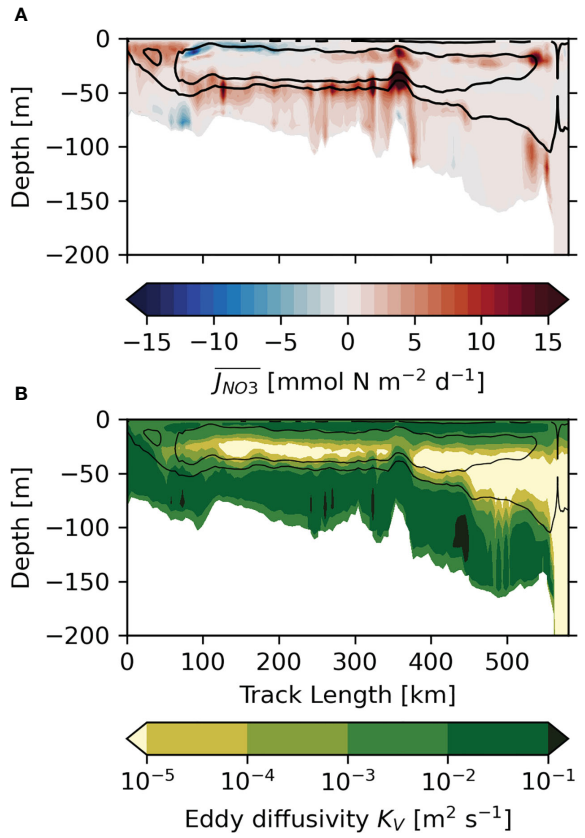

FIGURE 9
Vertical transect from Irish Sea (52.63°N, 5.49°W) to Celtic Sea shelf break (48.11°N, 9.54°W) of **(A)** the difference (TIDE−NOTIDE) of the mean turbulent nitrate flux, $\Delta\,\overline{J_{NO3}}$, during the period of strongest stratification (15 July −15 August, 2011–2015) and **(B)** corresponding eddy diffusivity $\overline{K_V}$ from TIDE experiment. Transect is marked in Figure 1B. Black contours indicate pycnocline in TIDE experiment ($N^2 = 0.5 \cdot 10^{-3}\ s^{-2}$ and $N^2 = 2 \cdot 10^{-3}\ s^{-2}$).

NWES in Figure 10A and for the Celtic Sea in Figure 10C. To understand the impact of tides on vertical mixing, we further compute the difference between $\overline{J_{NO3}(z_N)}$ in the TIDE and NOTIDE experiments. The proportional difference between the two experiments, expressed as $\Delta\,\overline{J_{NO3}(z_N)}$, is shown in Figure 10B.

$\overline{J_{NO3}(z_N)}$ in Figure 10A, C is zero if there is no vertical nitrate gradient, like in the permanently mixed regions along the coasts. In the northeastern Celtic Sea, the fresh and nutrient-rich river outflow from the Bristol Channel obscures the mixing signal. Figure 10A shows that turbulent transports are high in the tidal frontal regions and weakly stratified shallow regions (delineated by PEA = 50 Jm^{-3} in Figure 10A). The high turbulent nutrient supply to the surface sustains particularly high NPP rates in the transitionary regimes, as can be seen by the spatial coherence of high NPP in Figure 6A and the high $\overline{J_{NO3}(z_N)}$ found along tidal frontal zones in the NWES (e.g., in the western English Channel or southern North Sea).

Turbulent nitrate fluxes across the nutricline are generally low in the stably stratified regions of the NWES (PEA > 50 Jm^{-3}). Figure 10A shows $\overline{J_{NO3}(z_N)} < 0.5$ mmol N m^{-2}d^{-1} in most of the central areas of the Celtic Sea and North Sea basins. Observations of diapycnal nutrient fluxes on the NWES are sparse and limited in time, making a direct comparison difficult. Observational estimates suggest a background flux of 1 – 2 mmol N m^{-2}d^{-1} for the wider Celtic Sea region (Sharples et al., 2001; Williams et al., 2013b). A general underestimation of pycnocline mixing in stratified shelf areas is common for turbulence closures like the GLS k–kl closure used in this study. The deficiency in the representation of pycnocline mixing is attributed to the fact that the parameterizations do not include all physical processes that contribute to pycnocline mixing on the shelf (Simpson et al., 1996; Rippeth, 2005). Observational estimates close to the Norwegian Trench region of the North Sea (< 0.5 mmol N m^{-2}d^{-1}; Bendtsen and Richardson, 2018) and the Western Irish Sea (0.31 mmol N m^{-2}d^{-1}; Williams et al., 2013a) however fit better with the mixing reproduced by the model.

The difference in $\overline{J_{NO3}(z_N)}$ between the NOTIDE and TIDE experiments in Figure 10B shows that tidal impacts explain almost all turbulent mixing across the nutricline in the shallow stratified regions of the NWES and a relevant proportion of $\overline{J_{NO3}(z_N)}$ in the central basins of the North Sea and Celtic Sea. Tidal impacts on $\overline{J_{NO3}(z_N)}$ clearly depend on local water depths and mirror the decreasing positive tidal NPP response with water depths in Figure 6B. $\overline{J_{NO3}(z_N)}$ decreases with water depths as mixing driven by the barotropic tide loses the potential to affect the euphotic zone. To effectively differentiate between turbulent mixing induced by the barotropic tide and by baroclinic processes like internal tides, we compute the distance ΔZ_{NB} between the nutricline, as a proxy for the euphotic depth, and the depth at which the eddy diffusivity $\overline{K_V}$ falls below $10^{-3}\ m^2 s^{-1}$ in the bottom layer as a proxy for the extent of the bottom boundary layer.

Figure 10D shows mean ΔZ_{NB} on the NWES for the period of maximum stratification from the 15 July to 15 August (mean for 2011–2015). The visual comparison with $\Delta\,\overline{J_{NO3}(z_N)}$ in Figure 10B indicates that in the North Sea, where there is low internal tide activity, ΔZ_{NB} = 30m approximately concurs with the extent of positive (i.e., tide-induced) $\Delta\,\overline{J_{NO3}(z_N)}$. The comparison with the tidal NPP response in Figure 6B supports this assumption; here, ΔZ_{NB} = 30m approximately corresponds to the boundary of the positive tidal NPP response. We use this simplified approximation to define that at $\Delta Z_{NB} > 30$m , the impact of the barotropic tide on pycnocline mixing becomes negligible and baroclinic processes like internal tides are the dominant drivers of pycnocline mixing.

As already indicated in Figure 9A, turbulent nitrate fluxes across the nutricline are enhanced in a distinct band along the Celtic Sea shelf break (Figures 10A–C). The barotropic tide plays a role in the EC tidal flux window (5.5 – 8.5°W), where tidal energy dissipation is very high (Pingree et al., 1982) and $\Delta Z_{NB} < 30$m extends nearly up to the shelf break (Figure 10D). $\overline{J_{NO3}(z_N)}$ is particularly high at the shelf break part of the EC tidal flux window (locally up to 5mmol N/m^2 d). The remaining area of elevated $\overline{J_{NO3}(z_N)}$ along the shelf break shows pronounced separation of bottom and surface mixed layers ($\Delta Z_{NB} \gg 30m$). In the sector of the Celtic Sea shelf break north of 8.5°W, Figures 10A, C show elevated $\overline{J_{NO3}(z_N)}$ with values in the range of ~ 0.5 – 2 mmol N m^{-2}d^{-1}. Local mixing hotspots with $\overline{J_{NO3}(z_N)}$ of up to 5 mmol N m^{-2}d^{-1} are also evident on the northern sector of the Celtic Sea shelf break. The elevated average turbulent nitrate fluxes fit with the observed range of 1 – 9 mmol N m^{-2}d^{-1} reported for the northern sector of the Celtic Sea shelf break by Sharples et al. (2007). The area of tidally enhanced

10.3389/fmars.2023.1206062

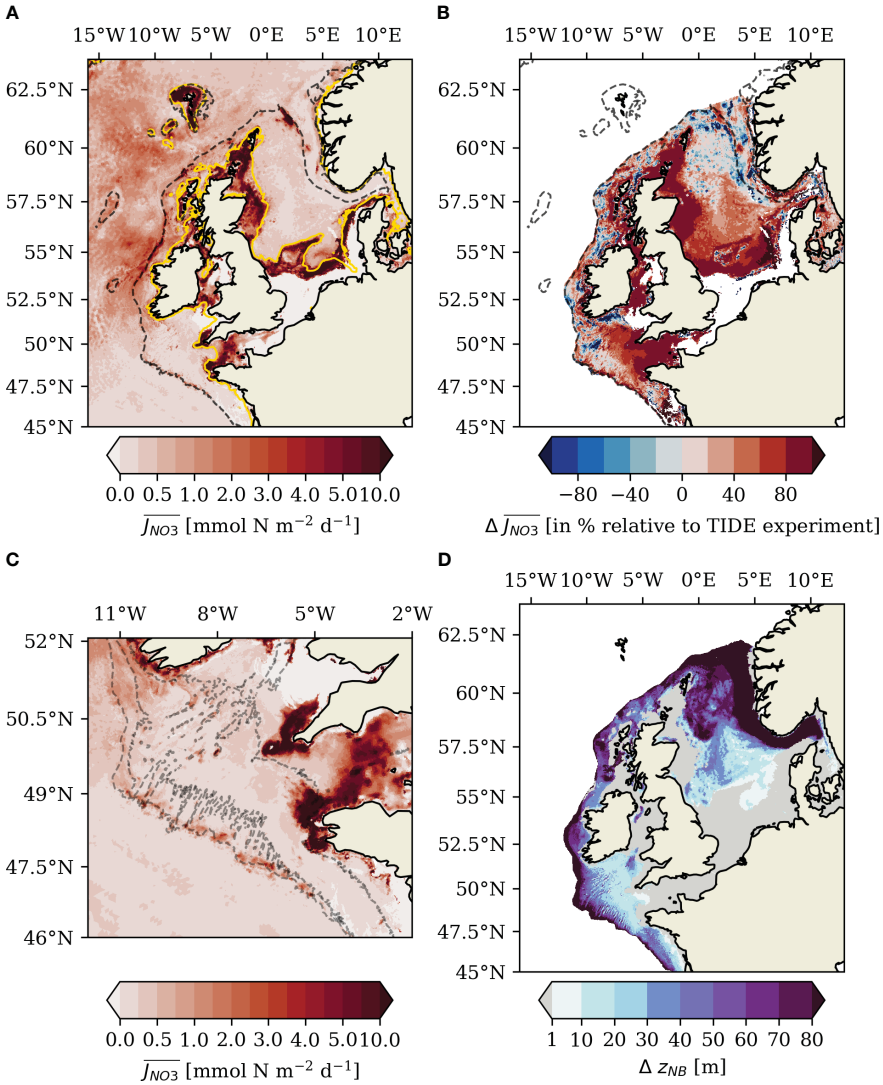

FIGURE 10
(A) Mean turbulent nitrate flux evaluated at nutricline, $\overline{J_{NO3}(z_N)}$, during period of strongest stratification (15 July – 15 August, mean for 2011–2015). Yellow contour in **(A)** shows *PEA* = 50 Jm^{-3}. **(B)** Proportional difference $\Delta\,\overline{J_{NO3}(z_N)}$ ([TIDE–NOTIDE]/TIDE) of the mean turbulent nitrate flux in percent relative to TIDE experiment. Areas where $\overline{J_{NO3}(z_N)}$ is zero masked for clarity. **(C)** $\overline{J_{NO3}(z_N)}$ during the period of strongest stratification (15 July – 15 August, mean for 2011–2015) in Celtic Sea. Dashed black contours indicate 100-, 150-, and 200-m isobaths. **(D)** Mean distance ΔZ_{NB} between the nutricline and the depth at which the eddy diffusivity $\overline{K_V}$ falls below 10^{-3} m^2s^{-1} in the bottom layer for 15 July – 15 August (mean for 2011–2015). Please note non-proportional colorbar discretization in **(A, C)**.

nitrate fluxes along the Celtic Sea shelf break in Figures 10A–C extends approximately 10–40 km onto the shelf. This also agrees with the observed dissipation of the majority of baroclinic energy within tens of kilometers of the generation site (Pingree et al., 1986; Inall et al., 2011).

Figure 10C further indicates elevated $\overline{J_{NO3}(z_N)}$ at small-scale bathymetric features throughout the Celtic Sea, with mean mixing rates of 0.5 – 3 mmol N m^{-2}d^{-1} at the respective ridges and sea banks. $\overline{J_{NO3}(z_N)}$ shown in Figure 10C reaches values of up to 10 mmol N m^{-2}d^{-1} at the distinct Jones Bank, which is well within the range of observed mixing rates attributed to local internal lee wave generation (Tweddle et al., 2013; 0.8 – 52 mmol N m^{-2}d^{-1}).

Background turbulent nitrate fluxes across the nutricline are overall higher on the narrow North-Western Approaches than in the southwestern Celtic Sea. Figure 10A shows elevated $\overline{J_{NO3}(z_N)}$ in some areas along the shelf break of the NWA where the surface and bottom layer are well separated ($\Delta Z_{NB} \gg$ 30m). $\overline{J_{NO3}(z_N)}$ is up to 15 mmol N m^{-2}d^{-1} along the shelf break northwest of Ireland at around 54.5 – 55.5°N, where upper-slope bathymetry is irregular and features a distinct canyon (Huthnance et al., 2022). $\overline{J_{NO3}(z_N)}$ is also elevated (1 – 4 mmol N m^{-2}d^{-1}, locally up to 18 mmol N/m^2 d) along the shelf break of and on the Malin Shelf at around 56 – 57°N, in an area where Figure 7B shows high internal tide activity and mixing by internal tides has been observed (Sherwin, 1988; Rippeth and Inall, 2002). A small area of high $\overline{J_{NO3}(z_N)}$ further occurs on the shelf break of Hebrides Shelf at around 7–8°W; here, Figure 10A shows values of up to 20 mmol N m^{-2}d^{-1}. $\overline{J_{NO3}(z_N)}$ on the northern North Sea shelf and shelf break is comparatively low.

Small patches of elevated $\overline{J_{NO3}(z_N)}$ with up to 5 mmol N $m^{-2}d^{-1}$ occur at the shelf break north of the Fair Isle Channel and the Shetland islands. A small area at northwestern edge of the Norwegian Trench potentially affected by the low salinity Baltic Sea outflow also shows $\overline{J_{NO3}(z_N)}$ of up to 20 mmol N $m^{-2}d^{-1}$.

The impact of the barotropic tide in the deep regions along the shelf break of the NWES is negligible ($\Delta Z_{NB} \gg$ 30m in Figure 10D). Figure 10B nevertheless shows that tidal forcing accounts for >60% of locally elevated $\overline{J_{NO3}(z_N)}$ in the region along the Celtic Sea shelf break during the investigated period of strongest stratification. Tidal forcing also accounts for >40%–60% of the locally elevated $\overline{J_{NO3}(z_N)}$ on the Malin Shelf. Positive $\Delta\,\overline{J_{NO3}(z_N)}$ further correlates with elevated $\overline{J_{NO3}(z_N)}$ on the northern flank of the Porcupine Bank, the Hebrides Shelf at around 7–8°W and the shelf break section north of the Fair Isle Channel. Sites of positive $\Delta\,\overline{J_{NO3}(z_N)}$ generally feature relevant internal tide activity (Figure 7B), whereas regions of low internal tide activity along the shelf break of the NWES partially feature low or negative $\Delta\,\overline{J_{NO3}(z_N)}$. The finding that $\Delta\,\overline{J_{NO3}(z_N)}$ predominantly explains locally elevated $\overline{J_{NO3}(z_N)}$ along the shelf break and the coherence with sites of high internal tide activity shows that the vertical mixing along the shelf break is caused by the resolved kilometrical-scale internal tide field in the region. The dissipation of on-shelf propagating low-mode internal tides vertically mixes nutrients into the euphotic zone and can contribute to the positive tidal NPP response identified for the shelf break regions in Figures 6B–D.

The emergence of substantially tidally elevated pycnocline mixing rates in proximity to internal tide generation sites suggests that resolving kilometrical-scale internal tides locally reduces the mid-water mixing deficiency commonly identified for stratified shelf regimes in ocean models (Simpson et al., 1996; Burchard et al., 2002; Rippeth, 2005). Our results here support Graham et al. (2018a), who suggested that a reduction of a warm SST bias along the Celtic Sea shelf break in their kilometrical-scale AMM15 NEMO model configuration was due to enhanced mixing by resolved internal tides. Pycnocline mixing simulated with a hydrostatic model like SCHISM will still likely underestimate mixing by the fully non-hydrostatic internal wave field (Vlasenko et al., 2014). Our results thus only constitute a lower bound for the impact of internal tides on shelf primary production. An improved representation of the non-linear interaction of wind-generated inertial oscillations and internal tides would also further improve the parameterization of the magnitude and episodic nature of mixing within the pycnocline (Davies and Xing, 2003; Hopkins et al., 2014), with potential impacts in central shelf areas as well. The representation and potentials for such non-linear interaction in kilometrical-scale regional ocean models is particularly interesting in this regard.

3.5 Impact of tide-generated pycnocline mixing on summer primary productivity

We further assess the contribution of tide-induced vertical mixing to the overall tidal NPP response in summer for the shelf areas along the shelf break. We compute tidally generated potential new production (PNP; Eq. 6) using the sum of tide-generated mean turbulent nitrate fluxes across the nutricline, i.e., $\Delta J_{NO3}(z_N)$, over the summer months (JJA; mean for 2011–2015). We only consider stably stratified areas with PEA > 50 Jm^{-3}, which explicitly excludes the tidal frontal areas. We further isolate the contribution of the internal-tide field from $\Delta J_{NO3}(z_N)$ by masking regions with ΔZ_{NB} < 30m and only considering the shelf area resolved at kilometrical-scale horizontal resolution. The results are summarized in Table 3.

Tide-generated potential new production sustained by vertical mixing across the pycnocline explains 20% (0.23 Mt C) of the mean tidal summer NPP response (JJA; 2011–2015) in the SWC subarea, with around 50% of PNP attributable to mixing by the internal tide alone (Table 3). Tide-generated pycnocline mixing in summer therefore only sustains ~ 3% of mean annual primary production in the SWC subarea. The remaining difference in mean summer NPP between the TIDE and NOTIDE experiments in the southwest Celtic Sea (0.92 Mt C; 80%) suggests that other tidally modulated processes are relevant for local primary production as well.

An intensification of regenerated primary production in the surface layer with tidal forcing, potentially associated with the delay of the spring bloom with tidal forcing (see Sect. 3.2) or re-entrainment of organic matter into the surface layer, could also play a role in the tidal NPP response in the Celtic Sea. Huthnance et al. (2022) further showed baroclinic on-shelf transport by internal tides at mooring stations at the Celtic Sea shelf break in summer. Graham et al. (2018b) also found substantial on-shelf transports along the pycnocline and in the surface layer at the Celtic Sea shelf break in late spring and summer and attributed the on-

TABLE 3 Overview of tidal impacts on summer net primary production in subareas along the shelf break.

Subarea	Internal-tide-generated summer PNP	Tide-generated summer PNP	Tidal summer NPP response	Ratio of tide-generated PNP to tidal summer NPP response
	[*Mt C*]	[*Mt C*]	[*Mt C*]	
SWC	0.12	0.23	1.15	20%
MS	0.03	0.08	0.08	92%
HS	0.03	0.06	0.09	65%
NNS	0.04	0.04	0.13	30%

Only stably stratified (PEA > 50 Jm^{-3}) segments of the subareas are considered. Tidal summer NPP response is computed as the sum of vertically integrated mean NPP for summer months (JJA; 2011–2015). Potential new production (PNP) is calculated with Eq. 6 using the sum of mean summer (JJA; 2011–2015) tide-generated turbulent nitrate fluxes across nutricline ($\Delta\,\overline{J_{NO3}(z_N)}$). Isolation of internal-tide-generated PNP is described in Sect. 3.5.

shelf transport at internal depths to internal tides resolved in their kilometrical-scale NEMO AMM15 model configuration. Tide-driven on-shelf transport would explain higher early summer nutrient concentrations in the TIDE experiment found in the outer shelf regions along the Celtic Sea shelf break for both the surface layer (>20 m; Figure 8A) and at internal depths (20–100 m; Figure 8B) in our study. In combination, the increased lateral on-shelf transport of nutrients from the tidally enhanced shelf break front (Figures 6B , 8A) and vertical mixing by internal tides likely account for the majority of the tidal response of summer NPP in the region. Recent work by Tinker et al. (2022) has also shown an impact of tidal forcing on the residual circulation on the NWES, with a pronounced tidal impact on the continental slope current. Tidal flow can additionally influence local circulation through topographically driven residual eddies, which are resolved at kilometrical-scale horizontal resolution in the Celtic Sea (Polton, 2015). Changes in the residual circulation potentially affect the nutrient distribution and biological productivity in the southwestern Celtic Sea. A detailed analysis of the different tidal impacts on cross-shelf horizontal transports is however beyond the scope of this study.

Analysis of potential new production driven by vertical mixing is more complex on the narrow shelves of the North-Western Approaches. The surface layer on the North-Western Approaches is not nutrient depleted in summer (Savidge and Lennon, 1987; Painter et al., 2017) because of cross-shelf exchange with nutrient-rich North Atlantic current water masses and upwelling at the shelf break (Huthnance et al., 2022). The persistent availability of nutrients in the surface layer throughout summer effectively limits the local NPP response to additional nutrient supply by tidal processes, which is particularly evident in tidal frontal zones (see Figure 6B). Table 3 nevertheless shows that tide-generated potential new production supplied by vertical mixing across the pycnocline can explain most of the low tidal response of summer NPP in the stratified areas of the Malin Shelf (92%) and Hebrides Shelf (65%). Tide-generated potential new production however only accounts for 30% of the tidal summer NPP response in the northern North Sea, suggesting relevant contributions of other tidally modulated processes here as well.

4 Conclusions

We introduce the flexible SCHISM-ECOSMO NWES-IT configuration and apply it to quantify the impact of barotropic and baroclinic tides on primary production on the NWES. The model validation demonstrates the reasonable simulation of the general hydrography and relevant biogeochemical cycles on the NWES. The applied strategy of local grid refinement shows high efficiency in computational cost and storage requirements, as the number of grid nodes is reduced by a factor of ~6 compared with a uniform high-resolution configuration. This makes the NWES-IT configuration a powerful tool for the investigation of kilometrical-scale physical processes relevant for shelf ecosystems and the continental shelf carbon pump.

Our results suggest that tidal forcing increases biological productivity on the NWES and that around 16% (14.47 Mt C) of annual mean primary production on the shelf is related to tidal forcing. Our study explored the hydrodynamic control of primary production on the shelf and identified a dominant role of tides for structuring primary production in shallow inner shelf regions like the southern and central North Sea, the English Channel, and the Irish Sea. Vertical mixing of nutrients by the barotropic tide particularly invigorates primary production in the tidal frontal regions of the NWES. Tidal mixing and the resuspension of suspended matter however also decrease primary production in shallow permanently mixed regions of the NWES.

A substantial increase of mean annual primary productivity by +25% (1.53 Mt C) was shown for the deep southwestern Celtic Sea. Tidal forcing mainly enhanced NPP in the southwestern Celtic Sea during the summer productive period. Tide-generated turbulent nutrient mixing across the pycnocline explains approximately one-fifth of the tidal response of summer NPP in the southwestern Celtic Sea. The overall contribution of tide-generated pycnocline mixing to mean annual primary production in the southwestern Celtic Sea is small (only around ~3%). Around 50% of the tide-generated pycnocline mixing in the southwestern Celtic Sea is attributed to the kilometrical-scale internal tide field resolved in the NWES-IT configuration. The large unaccounted remainder of the tidal response of summer NPP found in this study suggests that the tidal NPP response in the southwestern Celtic Sea is caused by a combination of processes. The enhancement of lateral on-shelf transport by tidal forcing, e.g., by internal tides along the pycnocline, is likely particularly important for primary production in the southwestern Celtic Sea. Tidal forcing only plays a minor role for primary production along the shelf break of the North-Western Approaches and the northern North Sea. The high productivity in these regions is rather due to nutrients supplied by cross-shelf exchange with nutrient-rich North Atlantic current water masses and upwelling at the shelf break.

Tidally enhanced turbulent mixing of nutrients across the pycnocline will likely affect the f ratio of summer primary production in the stratified regions of the NWES. The f ratio, which is the rate of new production to total primary production, is a relevant control for the oceanic uptake of atmospheric CO_2. A tidally enhanced biological carbon pump may increase sequestration of atmospheric CO_2 in shelf sediments or *via* off-shelf transport in the continental shelf carbon pump. As much of the tidal NPP response occurs in the frontal areas of the NWES, the particular dynamics of primary production in and adjacent to tidal fronts merit careful consideration in future work on the shelf carbon cycle. The substantial overall tidal impact on primary production on the NWES could potentially lead to a contribution of long-term tidal variations (e.g., the 18.61-year nodal cycle or the 8.85-year lunar perigee cycle) to long-term variability of marine ecosystem dynamics and oceanic CO_2 uptake.

The significant contribution of the barotropic and baroclinic tide to primary production on the NWES identified in this study further underlines the need to accurately assess and constrain tidal impacts on oceanic uptake of atmospheric CO_2. Further research

should also address the potential sensitivity of pycnocline mixing to the increase in thermal stratification in a warming climate (Holt et al., 2010; Mathis et al., 2019). The impact of barotropic and baroclinic tides on primary production found in this study moreover highlights the necessity of their representation in regional and global ocean models. This particularly applies to modeling studies that address regional and global marine carbon cycle dynamics. Kilometrical-scale horizontal resolution will likely remain beyond computational feasibility for large-scale model applications in the near future, although advances in model development were recently made to overcome such conceptual limitations (Mathis et al., 2022). Therefore, further work is required to improve the parameterization of kilometrical-scale physical processes like internal tides.

Data availability statement

The raw data supporting the conclusions of this article will be made available by the authors, without undue reservation.

Author contributions

JK generated the data set, performed the data analysis, and wrote the manuscript. MM, YZ, and CS provided essential background knowledge and advised the study. CS initiated the idea of the study. All authors contributed to conception and design of the study and manuscript revision, and read and approved the submitted version.

Acknowledgments

We would like to acknowledge the contribution by Richard Hofmeister to the development of SCHISM–ECOSMO. We would like to thank Benjamin Jacob and Johannes Pein for helpful advice regarding the SCHISM model. Computational resources were made available by the German Climate Computing Center (DKRZ) through support from the German Federal Ministry of Education and Research (BMBF). We would like to thank the reviewers for their time and insights. They have helped improve the manuscript. We would like to thank ICDC, CEN, University Hamburg, for data support. This study has been conducted using E.U. Copernicus Marine Service Information; https://doi.org/10.48670/moi-00169; http://dx.doi.org/10.17183/REFMAR; https://doi.org/10.48670/moi-00281. The manuscript contains data supplied by the Natural Environmental Research Council (NERC). The tidal validation and analysis in this manuscript used tools and open data sets made publicly available under a CECILL license at https://github.com/KarenGuihou/tidal_analysis. The research was funded by the Deutsche Forschungsgemeinschaft (DFG, German Research Foundation) under Germany's Excellence Strategy – EXC 2037 'CLICCS - Climate, Climatic Change, and Society' – Project Number: 390683824 and contributes to the CLICCS subproject A5 – The Land-Ocean Transition Zone. The article processing charges for this open-access publication were covered by the Helmholtz-Zentrum Hereon.

Conflict of interest

The authors declare that the research was conducted in the absence of any commercial or financial relationships that could be construed as a potential conflict of interest.

Publisher's note

All claims expressed in this article are solely those of the authors and do not necessarily represent those of their affiliated organizations, or those of the publisher, the editors and the reviewers. Any product that may be evaluated in this article, or claim that may be made by its manufacturer, is not guaranteed or endorsed by the publisher.

Supplementary material

The Supplementary Material for this article can be found online at: https://www.frontiersin.org/articles/10.3389/fmars.2023.1206062/full#supplementary-material

References

Allen, J. I., Holt, J. T., Blackford, J., and Proctor, R. (2007). Error quantification of a high-resolution coupled hydrodynamic-ecosystem coastal-ocean model: part 2. chlorophyll-a, nutrients and SPM. *J. Mar. Syst.* 68, 381–404. doi: 10.1016/j.jmarsys.2007.01.005

Aquaveo, L. L. C. (2019). *Surface-water modeling system: reference manual & tutorials* (LLC, Provo, Utah: Aquaveo LLC).

Baines, P. G. (1982). On internal tide generation models. *Deep Sea Res. Part A. Oceanographic Res. Papers* 29, 307–338. doi: 10.1016/0198-0149(82)90098-X

Becherer, J., Burchard, H., Carpenter, J. R., Graewe, U., and Merckelbach, L. M. (2022). The role of turbulence in fueling the subsurface chlorophyll maximum in tidally dominated shelf seas. *J. Geophys. Res. Oceans* 127, e2022JC018561. doi: 10.1029/2022JC018561

Bendtsen, J., and Richardson, K. (2018). Turbulence measurements suggest high rates of new production over the shelf edge in the Northeastern North Sea during summer. *Biogeosciences* 15, 7315–7332. doi: 10.5194/bg-15-7315-2018

Blumberg, A. F., and Mellor, G. L. (1987). A description of a three-dimensional coastal ocean circulation model. In *Three-Dimensional Coastal Ocean Models*, N.S. Heaps (Ed.), 1–16. doi: 10.1029/CO004p0001

Boyer, T. P., García, H. E., Locarnini, R. A., Zweng, M. M., Mishonov, A. V., Reagan, J. R., et al. (2018) *World ocean atlas 2018*. Available at: https://www.ncei.noaa.gov/archive/accession/NCEI-WOA18 (Accessed 29, 2022).

Bruggeman, J., and Bolding, K. (2014). A general framework for aquatic biogeochemical models. *Environ. Model. Software* 61, 249–265. doi: 10.1016/j.envsoft.2014.04.002

Burchard, H., Bolding, K., Rippeth, T. P., Stips, A., Simpson, J. H., and Sündermann, J. (2002). Microstructure of turbulence in the Northern North Sea: a comparative study of observations and model simulations. *Processes Vertical Exchange Shelf Seas (PROVESS) Part I* 47, 223–238. doi: 10.1016/S1385-1101(02)00126-0

Caldwell, P. C., Merrifield, M. A., and Thompson, P. R. (2015)Sea Level measured by tide gauges from global oceans — the joint archive for Sea level holdings (NCEI accession 0019568): version 5.5. In: *Dataset* (Accessed 02, 2022).

Capuzzo, E., Lynam, C. P., Barry, J., Stephens, D., Forster, R. M., Greenwood, N., et al. (2018). A decline in primary production in the North Sea over 25 years, associated with reductions in zooplankton abundance and fish stock recruitment. *Global Change Biol.* 24, e352–e364. doi: 10.1111/gcb.13916

Capuzzo, E., Painting, S. J., Forster, R. M., Greenwood, N., Stephens, D. T., and Mikkelsen, O. A. (2013). Variability in the sub-surface light climate at ecohydrodynamically distinct sites in the North Sea. *Biogeochemistry* 113, 85–103. doi: 10.1007/s10533-012-9772-6

Cloern, J. E. (1991). Tidal stirring and phytoplankton bloom dynamics in an estuary. *J. Mar. Res.* 49, 203–221. doi: 10.1357/002224091784968611

Cullen, J. J. (2015). Subsurface chlorophyll maximum layers: enduring enigma or mystery solved? *Annu. Rev. Mar. Sci.* 7, 207–239. doi: 10.1146/annurev-marine-010213-135111

Daewel, U., and Schrum, C. (2013). Simulating long-term dynamics of the coupled North Sea and Baltic Sea ecosystem with ECOSMO II: model description and validation. *J. Mar. Syst.* 119-120, 30–49. doi: 10.1016/j.jmarsys.2013.03.008

Davies, A. M., and Xing, J. (2003). On the interaction between internal tides and wind-induced near-inertial currents at the shelf edge. *J. Geophys. Res.* 108(C3). doi: 10.1029/2002JC001375

Dugdale, R. C., and Goering, J. J. (1967). UPTAKE OF NEW AND REGENERATED FORMS OF NITROGEN IN PRIMARY PRODUCTIVITY1. *Limnol. Oceanogr.* 12, 196–206. doi: 10.4319/lo.1967.12.2.0196

Fofonoff, N. P., and Millard, R. C. (1983). Algorithms for computation of fundamental properties of seawater. *Unesco Tech. papers Mar. Sci.* 44. doi: 10.25607/OBP-1450

Frankignoulle, M., and Borges, A. V. (2001). European Continental shelf as a significant sink for atmospheric carbon dioxide. *Global Biogeochem. Cycles* 15, 569–576. doi: 10.1029/2000GB001307

Geyer, B. (2017). *coastDat-3_COSMO-CLM_ERAi* (World Data Center for Climate (WDCC) at DKRZ). Available at: http://cera-www.dkrz.de/WDCC/ui/Compact.jsp?acronym=coastDat-3_COSMO-CLM_ERAi.

Graham, J. A., O'Dea, E., Holt, J., Polton, J., Hewitt, H. T., Furner, R., et al. (2018a). AMM15: a new high-resolution NEMO configuration for operational simulation of the European north-west shelf. *Geosci. Model. Dev.* 11, 681–696. doi: 10.5194/gmd-11-681-2018

Graham, J. A., Rosser, J. P., O'Dea, E., and Hewitt, H. T. (2018b). Resolving shelf break exchange around the European Northwest shelf. *Geophys. Res. Lett.* 45, 12,386–12,395. doi: 10.1029/2018GL079399

Green, J. A. M., Simpson, J. H., Legg, S., and Palmer, M. R. (2008). Internal waves, baroclinic energy fluxes and mixing at the European shelf edge. *Continental Shelf Res.* 28, 937–950. doi: 10.1016/j.csr.2008.01.014

Guihou, K., Polton, J., Harle, J., Wakelin, S., O'Dea, E., and Holt, J. (2018). Kilometric scale modeling of the North West European shelf seas: exploring the spatial and temporal variability of internal tides. *J. Geophys. Res. Oceans* 123, 688–707. doi: 10.1002/2017JC012960

Hall, R. A., Berx, B., and Damerell, G. M. (2019). Internal tide energy flux over a ridge measured by a co-located ocean glider and moored acoustic Doppler current profiler. *Ocean Sci.* 15, 1439–1453. doi: 10.5194/os-15-1439-2019

Hickman, A. E., Moore, C. M., Sharples, J., Lucas, M. I., Tilstone, G. H., Krivtsov, V., et al. (2012). Primary production and nitrate uptake within the seasonal thermocline of a stratified shelf sea. *Mar. Ecol. Prog. Ser.* 463, 39–57. doi: 10.3354/meps09836

Hinrichs, I., and Gouretski, V. (2019). *Baltic And north Sea climatology hydrographic part (Version 1.1)* (World Data Center for Climate (WDCC) at DKRZ). doi: 10.26050/WDCC/BNSClimHydrov1.1

Hofmeister, R., Flöser, G., and Schartau, M. (2017). Estuary-type circulation as a factor sustaining horizontal nutrient gradients in freshwater-influenced coastal systems. *Geo-Marine Lett.* 37, 179–192. doi: 10.1007/s00367-016-0469-z

Holt, J., Butenschön, M., Wakelin, S. L., Artioli, Y., and Allen, J. I. (2012). Oceanic controls on the primary production of the Northwest European continental shelf: model experiments under recent past conditions and a potential future scenario. *Biogeosciences* 9, 97–117. doi: 10.5194/bg-9-97-2012

Holt, J., Schrum, C., Cannaby, H., Daewel, U., Allen, I., Artioli, Y., et al. (2016). Potential impacts of climate change on the primary production of regional seas: a comparative analysis of five European seas. *Prog. IN OCEANOGRAPHY* 140, 91–115. doi: 10.1016/j.pocean.2015.11.004

Holt, J., and Umlauf, L. (2008). Modelling the tidal mixing fronts and seasonal stratification of the Northwest European continental shelf. *Continental Shelf Res.* 28, 887–903. doi: 10.1016/j.csr.2008.01.012

Holt, J., Wakelin, S., Lowe, J., and Tinker, J. (2010). The potential impacts of climate change on the hydrography of the Northwest European continental shelf. *Prog. IN OCEANOGRAPHY* 86, 361–379. doi: 10.1016/j.pocean.2010.05.003

Hopkins, J. E., Stephenson, G. R., Green, J. A. M., Inall, M. E., and Palmer, M. R. (2014). Storms modify baroclinic energy fluxes in a seasonally stratified shelf sea: inertial-tidal interaction. *J. Geophys. Res. Oceans* 119, 6863–6883. doi: 10.1002/2014JC010011

Hu, S., Townsend, D. W., Chen, C., Cowles, G., Beardsley, R. C., Ji, R., et al. (2008). Tidal pumping and nutrient fluxes on georges bank: a process-oriented modeling study. *J. Mar. Syst.* 74, 528–544. doi: 10.1016/j.jmarsys.2008.04.007

Huthnance, J., Hopkins, J., Berx, B., Dale, A., Holt, J., Hosegood, P., et al. (2022). Ocean shelf exchange, NW European shelf seas: measurements, estimates and comparisons. *Prog. IN OCEANOGRAPHY* 202, 102760. doi: 10.1016/j.pocean.2022.102760

ICES (1983). Flushing times of the North Sea. *ICES Cooperative Res. Rep.* 123, 153.

Inall, M., Aleynik, D., Boyd, T., Palmer, M., and Sharples, J. (2011). Internal tide coherence and decay over a wide shelf sea. *Geophys. Res. Lett.* 38, n/a–n/a. doi: 10.1029/2011GL049943

Intergovernmental Oceanographic Commission (1985). "Manual on sea level measurement and interpretation," in *Volume I - basic procedures* (Paris, France: UNESCO) 1, 83. doi: 10.25607/OBP-1420

Joint, I., and Groom, S. B. (2000). Estimation of phytoplankton production from space: current status and future potential of satellite remote sensing. *J. Exp. Mar. Biol. Ecol.* 250, 233–255. doi: 10.1016/S0022-0981(00)00199-4

Joint, I., and Pomroy, A. (1993). PHYTOPLANKTON BIOMASS AND PRODUCTION IN THE SOUTHERN NORTH-SEA. *Mar. Ecol. Prog. Ser.* 99, 169–182. doi: 10.3354/meps099169

Joint, I., Wollast, R., Chou, L., Batten, S., Elskens, M., Edwards, E., et al. (2001). Pelagic production at the Celtic Sea shelf break. *DEEP-SEA Res. Part II-TOPICAL Stud. IN OCEANOGRAPHY* 48, 3049–3081. doi: 10.1016/S0967-0645(01)00032-7

Kamp, A., and Witte, U. (2005). Processing of 13C-labelled phytoplankton in a fine-grained sandy-shelf sediment (North Sea): relative importance of different macrofauna species. *Mar. Ecol. Prog. Ser.* 297, 61. doi: 10.3354/meps297061

Kantha, L. H., and Clayson, C. A. (1994). An improved mixed layer model for geophysical applications. *J. Geophys. Res.* 99, 25235–25266. doi: 10.1029/94JC02257

Laruelle, G. G., Lauerwald, R., Pfeil, B., and Regnier, P. (2014). Regionalized global budget of the CO2 exchange at the air-water interface in continental shelf seas. *Global Biogeochem. Cycles* 28, 1199–1214. doi: 10.1002/2014GB004832

Legge, O., Johnson, M., Hicks, N., Jickells, T., Diesing, M., Aldridge, J., et al. (2020). Carbon on the Northwest European shelf: contemporary budget and future influences. *Front. Mar. Sci.* 7. doi: 10.3389/fmars.2020.00143

Le Guitton, M., Soetaert, K., Sinninghe Damsté, J. S., and Middelburg, J. J. (2017). A seasonal study of particulate organic matter composition and quality along an offshore transect in the Southern North Sea. *Estuarine Coast. Shelf Sci.* 188, 1–11. doi: 10.1016/j.ecss.2017.02.002

Lin, L., Liu, H., Huang, X., Fu, Q., and Guo, X. (2022). Effect of tides on river water behavior over the eastern shelf seas of China. *Hydrology Earth System Sci.* 26, 5207–5225. doi: 10.5194/hess-26-5207-2022

Lyard, F. H., Allain, D. J., Cancet, M., Carrère, L., and Picot, N. (2021). FES2014 global ocean tide atlas: design and performance. *Ocean Sci.* 17, 615–649. doi: 10.5194/os-17-615-2021

Mann, K. H., and Lazier, J. R. (2013). *Dynamics of marine ecosystems: biological-physical interactions in the oceans. 3rd ed.* (John Wiley & Sons, Ltd).

Mathis, M., Elizalde, A., and Mikolajewicz, U. (2019). The future regime of Atlantic nutrient supply to the Northwest European shelf. *J. Mar. Syst.* 189, 98–115. doi: 10.1016/j.jmarsys.2018.10.002

Mathis, M., Logemann, K., Maerz, J., Lacroix, F., Hagemann, S., Chegini, F., et al. (2022). Seamless integration of the coastal ocean in global marine carbon cycle modeling. *J. Adv. Model. Earth Syst.* 14, e2021MS002789. doi: 10.1029/2021MS002789

New, A. L., and Pingree, R. D. (1990). Evidence for internal tidal mixing near the shelf break in the bay of Biscay. *Deep Sea Res. Part A. Oceanographic Res. Papers* 37, 1783–1803. doi: 10.1016/0198-0149(90)90078-A

Nissen, C. (2014). *Physical-biogeochemical couplings in the land-ocean transition zone* (Bergen: The University of Bergen).

O'Dea, E. J., Arnold, A. K., Edwards, K. P., Furner, R., Hyder, P., Martin, M. J., et al. (2012). An operational ocean forecast system incorporating NEMO and SST data assimilation for the tidally driven European North-West shelf. *J. OF OPERATIONAL OCEANOGRAPHY* 5, 3–17. doi: 10.1080/1755876X.2012.11020128

Painter, S. C., Hartman, S. E., Kivimäe, C., Salt, L. A., Clargo, N. M., Daniels, C. J., et al. (2017). The elemental stoichiometry (C, Si, n, p) of the Hebrides shelf and its role in carbon export. *Prog. IN OCEANOGRAPHY* 159, 154–177. doi: 10.1016/j.pocean.2017.10.001

Palmer, M. R., Inall, M. E., and Sharples, J. (2013). The physical oceanography of Jones bank: a mixing hotspot in the Celtic Sea. *Prog. IN OCEANOGRAPHY* 117, 9–24. doi: 10.1016/j.pocean.2013.06.009

Pätsch, J., Burchard, H., Dieterich, C., Gräwe, U., Gröger, M., Mathis, M., et al. (2017). An evaluation of the North Sea circulation in global and regional models relevant for ecosystem simulations. *Ocean Model.* 116, 70–95. doi: 10.1016/j.ocemod.2017.06.005

Pein, J., Eisele, A., Sanders, T., Daewel, U., Stanev, E. V., van Beusekom, J. E. E., et al. (2021). Seasonal stratification and biogeochemical turnover in the freshwater reach of a partially mixed dredged estuary. *Front. Mar. Sci.* 8. doi: 10.3389/fmars.2021.623714

Pingree, R. D., and Mardell, G. T. (1981). Slope turbulence, internal waves and phytoplankton growth at the Celtic Sea shelf-break. *Philos. Trans. R. Soc. London. Ser. A Math. Phys. Sci.* 302(1472), 663–682. doi: 10.1098/rsta.1981.0191

Pingree, R. D., and Mardell, G. T. (1985). Solitary internal waves in the Celtic Sea. *Prog. IN OCEANOGRAPHY* 14, 431–441. doi: 10.1016/0079-6611(85)90021-7

Pingree, R. D., Mardell, G. T., Holligan, P. M., Griffiths, D. K., and Smithers, J. (1982). Celtic Sea and armorican current structure and the vertical distributions of temperature and chlorophyll. *Continental Shelf Res.* 1, 99–116. doi: 10.1016/0278-4343(82)90033-4

Pingree, R. D., Mardell, G. T., and New, A. L. (1986). Propagation of internal tides from the upper slopes of the bay of Biscay. *Nature* 321, 154–158. doi: 10.1038/321154a0

Pingree, R. D., and New, A. L. (1995). Structure, seasonal development and sunglint spatial coherence of the internal tide on the celtic and armorican shelves and in the bay of Biscay. *Deep Sea Res. Part I: Oceanographic Res. Papers* 42, 245–284. doi: 10.1016/0967-0637(94)00041-P

Pingree, R. D., Pugh, P. R., Holligan, P. M., and Forster, G. R. (1975). Summer phytoplankton blooms and red tides along tidal fronts in the approaches to the English channel. *Nature* 258, 672–677. doi: 10.1038/258672a0

Polton, J. A. (2015). Tidally induced mean flow over bathymetric features: a contemporary challenge for high-resolution wide-area models. *Geophysical Astrophysical Fluid Dynamics* 109, 207–215. doi: 10.1080/03091929.2014.952726

Porter, E. T., Mason, R. P., and Sanford, L. P. (2010). Effect of tidal resuspension on benthic–pelagic coupling in an experimental ecosystem study. *Mar. Ecol. Prog. Ser.* 413, 33–53. doi: 10.3354/meps08709

Prins, T., Smaal, A. C., Pouwer, A. J., and Dankers, N. (1996). Filtration and resuspension of particulate matter and phytoplankton on an intertidal mussel bed in the oosterschelde estuary (SW Netherlands). *Mar. Ecol. Prog. Ser.* 142, 121–134. doi: 10.3354/meps142121

Richardson, K., Visser, A. W., and Pedersen, F. B. (2000). Subsurface phytoplankton blooms fuel pelagic production in the North Sea. *J. Plankton Res.* 22, 1663–1671. doi: 10.1093/plankt/22.9.1663

Rippeth, T. P. (2005). Mixing in seasonally stratified shelf seas: a shifting paradigm. *Philos. Trans. Ser. A Mathematical physical Eng. Sci.* 363, 2837–2854. doi: 10.1098/rsta.2005.1662

Rippeth, T. P., and Inall, M. E. (2002). Observations of the internal tide and associated mixing across the malin shelf. *J. Geophys. Res.* 107, 928. doi: 10.1029/2000JC000761

Rippeth, T. P., Lincoln, B. J., Kennedy, H. A., Palmer, M. R., Sharples, J., and Williams, C. A. J. (2014). Impact of vertical mixing on sea surface pCO2 in temperate seasonally stratified shelf seas. *J. Geophys. Res. Oceans* 119, 3868–3882. doi: 10.1002/2014JC010089

Rippeth, T. P., Wiles, P., Palmer, M. R., Sharples, J., and Tweddle, J. (2009). The diapcynal nutrient flux and shear-induced diapcynal mixing in the seasonally stratified Western Irish Sea. *Continental Shelf Res.* 29, 1580–1587. doi: 10.1016/j.csr.2009.04.009

Samuelsen, A., Schrum, C., Yumruktepe, V.Ç., Daewel, U., and Roberts, E. M. (2022). Environmental change at deep-Sea sponge habitats over the last half century: a model hindcast study for the age of anthropogenic climate change. *Front. Mar. Sci.* 9. doi: 10.3389/fmars.2022.737164

Savidge, G., and Lennon, H. J. (1987). Hydrography and phytoplankton distributions in North-west Scottish waters. *Continental Shelf Res.* 7, 45–66. doi: 10.1016/0278-4343(87)90063-X

Schrum, C., Alekseeva, I., and St. John, M. (2006). Development of a coupled physical–biological ecosystem model ECOSMO. *J. Mar. Syst.* 61, 79–99. doi: 10.1016/j.jmarsys.2006.01.005

Sharples, J. (2008). Potential impacts of the spring-neap tidal cycle on shelf sea primary production. *J. Plankton Res.* 30, 183–197. doi: 10.1093/plankt/fbm088

Sharples, J., Moore, C. M., Hickman, A. E., Holligan, P. M., Tweddle, J. F., Palmer, M. R., et al. (2009). Internal tidal mixing as a control on continental margin ecosystems. *Geophys. Res. Lett.* 36, 249. doi: 10.1029/2009GL040683

Sharples, J., Moore, M. C., Rippeth, T. P., Holligan, P. M., Hydes, D. J., Fisher, N. R., et al. (2001). Phytoplankton distribution and survival in the thermocline. *Limnol. Oceanogr.* 46, 486–496. doi: 10.4319/lo.2001.46.3.0486

Sharples, J., Tweddle, J. F., Mattias Green, J. A., Palmer, M. R., Kim, Y.-N., Hickman, A. E., et al. (2007). Spring-neap modulation of internal tide mixing and vertical nitrate fluxes at a shelf edge in summer. *Limnol. Oceanogr.* 52, 1735–1747. doi: 10.4319/lo.2007.52.5.1735

Sherwin, T. (1988). Analysis of an internal tide observed on the malin shelf, north of Ireland. *J. Phys. Oceanography - J. Phys. OCEANOGR* 18, 1035–1050. doi: 10.1175/1520-0485(1988)018<1035:AOAITO>2.0.CO;2

Sherwin, T. J. (1991). "Evidence of a deep internal tide in the Faeroe-Shetland channel," in *Tidal hydrodynamics*, vol. 469–488 . Ed. B. B. Parker (New York: John Wiley).

Simpson, J. H., Crawford, W. R., Rippeth, T. P., Campbell, A. R., and Cheok, J. V. S. (1996). The vertical structure of turbulent dissipation in shelf seas. *J. Phys. Oceanography* 26, 1579–1590. doi: 10.1175/1520-0485(1996)026<1579:TVSOTD>2.0.CO;2

Simpson, J. H., Crisp, D. J., Hearn, C., Swallow, J. C., Currie, R. I., and Gill, A. E. (1981). The shelf-sea fronts: implications of their existence and behaviour. *Philos. Trans. R. Soc. London. Ser. A Math. Phys. Sci.* 302, 531–546. doi: 10.1098/rsta.1981.0181

Simpson, J. H., and Hunter, J. R. (1974). Fronts in the Irish Sea. *Nature* 250, 404–406. doi: 10.1038/250404a0

Taylor, M. H., Akimova, A., Bracher, A., Kempf, A., Kühn, B., and Hélaouët, P. (2021). Using dynamic ocean color provinces to elucidate drivers of North Sea hydrography and ecology. *J. Geophys. Res. Oceans* 126, e2021JC017686. doi: 10.1029/2021JC017686

Tett, P., and Walne, A. (1995). Observations and simulations of hydrography, nutrients and plankton in the southern north Sea. *Ophelia* 42, 371–416. doi: 10.1080/00785326.1995.10431514

Thomas, H., Bozec, Y., Elkalay, K., and Baar, H.J.W.de (2004). Enhanced open ocean storage of CO2 from shelf sea pumping. *Sci. (New York N.Y.)* 304, 1005–1008. doi: 10.1126/science.1095491

Tinker, J., Polton, J. A., Robins, P. E., Lewis, M. J., and O'Neill, C. K. (2022). The influence of tides on the North West European shelf winter residual circulation. *Front. Mar. Sci.* 9. doi: 10.3389/fmars.2022.847138

Tsunogai, S., Watanabe, S., and Sato, T. (1999). Is there a "continental shelf pump" for the absorption of atmospheric CO2? *Tellus B* 51, 701–712. doi: 10.1034/j.1600-0889.1999.t01-2-00010.x

Tweddle, J. F., Sharples, J., Palmer, M. R., Davidson, K., and McNeill, S. (2013). Enhanced nutrient fluxes at the shelf sea seasonal thermocline caused by stratified flow over a bank. *Prog. IN OCEANOGRAPHY* 117, 37–47. doi: 10.1016/j.pocean.2013.06.018

Umlauf, L., and Burchard, H. (2003). A generic length-scale equation for geophysical turbulence models. *J. Mar. Res.* 61, 235–265. doi: 10.1357/002224003322005087

van Haren, H., Maas, L., Zimmerman, J. T. F., Ridderinkhof, H., and Malschaert, H. (1999). Strong inertial currents and marginal internal wave stability in the Central North Sea. *Geophys. Res. Lett.* 26, 2993–2996. doi: 10.1029/1999GL002352

van Leeuwen, S., Tett, P., Mills, D., and van der Molen, J. (2015). Stratified and nonstratified areas in the North Sea: long-term variability and biological and policy implications. *J. Geophys. Res. Oceans* 120, 4670–4686. doi: 10.1002/2014JC010485

Vlasenko, V., Stashchuk, N., Inall, M. E., and Hopkins, J. E. (2014). Tidal energy conversion in a global hot spot: on the 3-d dynamics of baroclinic tides at the Celtic Sea shelf break. *J. Geophys. Res. Oceans* 119, 3249–3265. doi: 10.1002/2013JC009708

Vlasenko, V., Stashchuk, N., Palmer, M. R., and Inall, M. E. (2013). Generation of baroclinic tides over an isolated underwater bank. *J. Geophys. Res. Oceans* 118, 4395–4408. doi: 10.1002/jgrc.20304

Wang, H., Gong, D., Friedrichs, M. A. M., Harris, C. K., Miles, T., Yu, H.-C., et al. (2022). A cycle of wind-driven canyon upwelling and downwelling at Wilmington canyon and the evolution of canyon-upwelled dense water on the MAB shelf. *Front. Mar. Sci.* 9. doi: 10.3389/fmars.2022.866075

Wang, Z., Li, D., Xue, H., Thomas, A. C., Zhang, Y. J., and Chai, F. (2022). Freshwater transport in the scotian shelf and its impacts on the gulf of Maine salinity. *JGR Oceans* 127, 16. doi: 10.1029/2021JC017663

Wessel, P., and Smith, W. H. F. (1996). A global, self-consistent, hierarchical, high-resolution shoreline database. *J. Geophys. Res.* 101, 8741–8743. doi: 10.1029/96JB00104

Whalen, C. B., Lavergne, C., Naveira Garabato, A. C., Klymak, J. M., MacKinnon, J. A., and Sheen, K. L. (2020). Internal wave-driven mixing: governing processes and consequences for climate. *Nat. Rev. Earth Environ.* 1, 606–621. doi: 10.1038/s43017-020-0097-z

Wihsgott, J., Hopkins, J., Sharples, J., Jones, E., and Balfour, C. (2016). Long-term mooring observations of full depth water column structure spanning 17 months, collected in a temperate shelf sea (Celtic Sea) British Oceanographic Data Centre - Natural Environment Research Council, UK. doi: 10.5285/389fe406-ebd9-74f1-e053-6c86abc032a4

Williams, C., Sharples, J., Green, M., Mahaffey, C., and Rippeth, T. (2013a). The maintenance of the subsurface chlorophyll maximum in the stratified Western Irish Sea. *Limnol. Oceanogr.* 3, 61–73. doi: 10.1215/21573689-2285100

Williams, C., Sharples, J., Mahaffey, C., and Rippeth, T. (2013b). Wind-driven nutrient pulses to the subsurface chlorophyll maximum in seasonally stratified shelf seas. *Geophys. Res. Lett.* 40, 5467–5472. doi: 10.1002/2013GL058171

Ye, F., Zhang, Y. J., He, R., Wang, Z., Wang, H. V., and Du, J. (2019). Third-order WENO transport scheme for simulating the baroclinic eddying ocean on an unstructured grid. *Ocean Model.* 143, 101466. doi: 10.1016/j.ocemod.2019.101466

Ye, F., Zhang, Y. J., Wang, H. V., Friedrichs, M. A., Irby, I. D., Alteljevich, E., et al. (2018). A 3D unstructured-grid model for Chesapeake bay: importance of bathymetry. *Ocean Model.* 127, 16–39. doi: 10.1016/j.ocemod.2018.05.002

Ye, F., Zhang, Y. J., Yu, H., Sun, W., Moghimi, S., Myers, E., et al. (2020). Simulating storm surge and compound flooding events with a creek-to-ocean model: importance of baroclinic effects. *Ocean Model.* 145, 101526. doi: 10.1016/j.ocemod.2019.101526

Yu, H.-C., Zhang, Y. J., Yu, J. C., Terng, C., Sun, W., Ye, F., et al. (2017). Simulating multi-scale oceanic processes around Taiwan on unstructured grids. *Ocean Model.* 119, 72–93. doi: 10.1016/j.ocemod.2017.09.007

Yumruktepe, V.Ç., Samuelsen, A., and Daewel, U. (2022). ECOSMO II(CHL): a marine biogeochemical model for the north Atlantic and the Arctic. *Geosci. Model. Dev.* 15, 3901–3921. doi: 10.5194/gmd-15-3901-2022

Zeng, X., Zhao, M., and Dickinson, R. E. (1998). Intercomparison of bulk aerodynamic algorithms for the computation of Sea surface fluxes using TOGA COARE and TAO data. *J. Climate* 11, 2628–2644. doi: 10.1175/1520-0442(1998)011%3C2628:IOBAAF%3E2.0.CO;2

Zhang, Y. J., Ateljevich, E., Yu, H.-C., Wu, C. H., and Yu, J. C. (2015). A new vertical coordinate system for a 3D unstructured-grid model. *Ocean Model.* 85, 16–31. doi: 10.1016/j.ocemod.2014.10.003

Zhang, Y., and Baptista, A. M. (2008). SELFE: a semi-implicit eulerian–Lagrangian finite-element model for cross-scale ocean circulation. *Ocean Model.* 21, 71–96. doi: 10.1016/j.ocemod.2007.11.005

Zhang, Y. J., Stanev, E. V., and Grashorn, S. (2016a). Unstructured-grid model for the North Sea and Baltic Sea: validation against observations. *Ocean Model.* 97, 91–108. doi: 10.1016/j.ocemod.2015.11.009

Zhang, Y. J., Ye, F., Stanev, E. V., and Grashorn, S. (2016b). Seamless cross-scale modeling with SCHISM. *Ocean Model.* 102, 64–81. doi: 10.1016/j.ocemod.2016.05.002

Zhao, C., Daewel, U., and Schrum, C. (2019). Tidal impacts on primary production in the North Sea. *Earth Syst. Dynam.* 10, 287–317. doi: 10.5194/esd-10-287-2019